2D Materials

ACCEPTED MANUSCRIPT • OPEN ACCESS

Graphene-Black Phosphorus Printed Photodetectors

To cite this article before publication: Shahab Akhavan *et al* 2023 *2D Mater.* in press https://doi.org/10.1088/2053-1583/acc74c

Manuscript version: Accepted Manuscript

Accepted Manuscript is "the version of the article accepted for publication including all changes made as a result of the peer review process, and which may also include the addition to the article by IOP Publishing of a header, an article ID, a cover sheet and/or an 'Accepted Manuscript' watermark, but excluding any other editing, typesetting or other changes made by IOP Publishing and/or its licensors"

This Accepted Manuscript is **© 2023 The Author(s). Published by IOP Publishing Ltd**.

As the Version of Record of this article is going to be / has been published on a gold open access basis under a CC BY 4.0 licence, this Accepted Manuscript is available for reuse under a CC BY 4.0 licence immediately.

Everyone is permitted to use all or part of the original content in this article, provided that they adhere to all the terms of the licence https://creativecommons.org/licences/by/4.0

Although reasonable endeavours have been taken to obtain all necessary permissions from third parties to include their copyrighted content within this article, their full citation and copyright line may not be present in this Accepted Manuscript version. Before using any content from this article, please refer to the Version of Record on IOPscience once published for full citation and copyright details, as permissions may be required. All third party content is fully copyright protected and is not published on a gold open access basis under a CC BY licence, unless that is specifically stated in the figure caption in the Version of Record.

View the article online for updates and enhancements.

This content was downloaded from IP address 129.169.232.75 on 27/03/2023 at 13:23

Graphene-Black Phosphorus Printed Photodetectors

S. Akhavan,[1,*] A. Ruocco,[1] G. Soavi,[1,†] A. Taheri Najafabadi,[1,‡] S. Mignuzzi,[1] S. Doukas,[2] A. R. Cadore,[1] Y. A. K. Samad,[1] L. Lombardi,[1] K. Dimos,[1] I. Paradisanos,[1] J. E. Muench,[1] H. F. Y. Watson,[1] S. Hodge,[1] L. G. Occhipinti,[1] E. Lidorikis,[2] I. Goykhman,[1,3] and A. C. Ferrari[1,§]

[1] *Cambridge Graphene Centre, University of Cambridge, Cambridge CB3 0FA, UK*
[2] *Department of Materials Science and Engineering, University of Ioannina, Ioannina 45110, Greece*
[3] *Technion - Israel Institute of Technology, Haifa 3200003, Israel*

Layered materials (LMs) produced by liquid phase exfoliation (LPE) can be used as building blocks for optoelectronic applications. However, when compared with mechanically exfoliated flakes, or films prepared by chemical vapor deposition (CVD), LPE-based printed optoelectronic devices are limited by mobility, defects and trap states. Here, we present a scalable fabrication technique combining CVD with LPE LMs to overcome such limitations. We use black phosphorus (BP) inks, inkjet-printed on graphene on Si/SiO_2, patterned by inkjet printing based lithography, and source and drain electrodes printed with an Ag ink, to prepare photodetectors (PDs). These have an external responsivity (R_{ext})$\sim$337A/W at 488nm, and operate from visible ($\sim$488nm) to short-wave infrared ($\sim$2.7μm, R_{ext} $\sim$48mA/W). We also use this approach to fabricate flexible PDs on polyester fabric, one of the most common used in textiles, achieving R_{ext} $\sim$6mA/W at 488nm for an operating voltage of 1V. Thus, our combination of scalable CVD and LPE techniques via inkjet printing is promising for wearable and flexible applications.

INTRODUCTION

Background

Photodetectors (PDs) are key components of video imaging[1], optical communications[2], night vision[3], gas sensing[4] and many other devices.

Their responsivity can be expressed as external[5, 6]:

$$R_{ext} = \frac{|I_{light} - I_{dark}|}{(P_{opt}.A_{PD}/A_{opt})} \quad (1)$$

or internal[6]:

$$R_{int} = \frac{|I_{light} - I_{dark}|}{(P_{abs}.A_{PD}/A_{opt})} \quad (2)$$

where I_{light} and I_{dark} are the currents of the PD under illumination and in dark conditions. A_{PD} and A_{opt} are the PD area and the laser spot size. A_{PD}/A_{opt} is a scaling factor that takes into account the fact that only a fraction of optical power impinges on the PD. P_{opt} is the incident optical power, and P_{abs}=$abs \times P_{opt}$ is the absorbed optical power, where 0< abs <1 is the optical absorption in the PD. Typically abs <1, since not all incident photons are absorbed ($P_{opt} > P_{abs}$)[6], therefore $R_{int} > R_{ext}$[6]. R_{ext} describes the overall PD responsivity, including device-related considerations, such as PD design and architecture, light absorption and reabsorption (i.e. the absorption of radiatively recombined photons in the PD photoactive materials), optical reflection from interfaces, optical path in the photoactive area, materials quality, etc.[6]. On the other hand, R_{int} provides an estimate of the photodetection efficiency, characterizing the optical-to-electrical conversion process of the absorbed photons[6]. R_{ext} is related to R_{int} as[6]:

$$R_{ext} = R_{int}.abs = \frac{\eta_{int} q \lambda abs(\lambda)}{hc} \quad (3)$$

where η_{int} is the internal quantum efficiency, i.e. the ratio of the number of charge carriers collected from the photoactive layer to the number of absorbed photons[6], q is the electron charge, λ is the incident light wavelength, h is the Planck constant, and c the speed of light. $abs(\lambda)$ is wavelength dependent, therefore the spectral response in quantum-type PDs (whereby photons generate electron-hole, e-h, pairs) typically follows the absorption spectrum of the light absorbing material[6].

The response time (τ_{life}) is the lifetime of the photogenerated charges in the light absorbing layer[5]. This determines the PD speed, defined as[5, 6]:

$$\tau_{life} = \frac{\Delta n}{QE \times \phi_{in}} \quad (4)$$

where Δn is the light-induced change in carrier density, QE is the external quantum efficiency, defined as QE=$\eta_{tran} \times \eta_{abs}$ where η_{tran} is the charge transfer efficiency (i.e. the ratio between the flux of charges that contribute to the current and the total light flux that reaches the surface), η_{abs} is the light absorption efficiency (i.e. the percentage of light transmitted from the sample), and ϕ_{in} is the incoming photon flux. The operation wavelength range is the spectral range where the PD is sensitive to incident light[6]. For cameras and video imaging, detection in the visible ($\sim$400-700nm) with τ_{life} $\sim$10-50ms is desired[5]. R_{ext} >0.1A/W can remove the need of amplifiers (to increase the output with respect to the input signal (i.e. current))[7], thus decreasing costs[7].

PDs currently in the market are mainly based on Si complementary metal–oxide–semiconductor (CMOS)

Accepted Manuscript

technology[8]. For applications in the short-wave infrared (SWIR) (1000-2500nm/1.24-0.5eV), beyond the Si bandgap (1.1eV)[6], current technology relies on III-V InGaAs PDs[9]. However, these require complex manufacturing steps (epitaxial growth)[10], cooling to liquid nitrogen[10] and they are rigid[10].

Layered materials-based photodetectors

Graphene and related materials (GRMs) are promising for PDs[5, 11], and have demonstrated R_{ext} $\sim 10^8$A/W at 532nm[12], with response time$\sim$ 10^{-4}s[13], 110GHz speed[14], operation wavelength covering visible to the mid-IR$\sim 3.2\mu$m[15] and THz[16, 17], and CMOS integrability[18]. Many GRM-based PDs fabricated based on scalable CVD approaches[19, 20] were also reported, with R_{ext} $\sim$121A/W at 532nm[20]. R_{ext} > 10^5A/W was achieved integrating graphene flakes[12] and/or layered materials (LMs), such as MoS_2,[21, 22] with PbS[23, 24] and HgTe quantum dots (QDs)[25], with spectral coverage determined by the absorption of the added material (e.g. QDs)[23].

In graphene-based PDs (e.g. metal-graphene-metal PDs[26]), $abs(\lambda)$ is governed by the wavelength dependent optical conductivity of SLG[27], doping[27], Pauli blocking[27], mobility[28], scattering time[29], device architecture, and substrate, which affects the optical path and the interference of the incident light[26]. In graphene PDs based on photogating (e.g. graphene/QDs[12], graphene/semiconductor[30]), abs(λ) depends on the absorption coefficient profile ($4\pi K/\lambda$)[6] of the light absorbing material, where K is the imaginary part of the photoactive material[6].

Liquid phase exfoliation (LPE) is a promising route for production of LM-based inks[31–36]. These have been used for printed solar cells[37], sensors[38], transistors[33], supercapacitors[39, 40], and PDs[41]. LPE inks were used to prepare PDs on rigid (e.g. Si)[42] and flexible (e.g. PET(polyethylene terephthalate))[43] substrates. Challenges in the development of inkjet-printed LPE based PDs stem from the limitations associated with the presence of traps (surface[44, 45] and interface sites[44, 45] formed during LPE), resulting in photocurrent loss[45].

PDs based on solution-synthesized MoS_2 on Si/SiO_2 were demonstrated[45]. These were prepared by dissolving $(NH_4)_2MoS_4$ in dimethylformamide:butylamine:aminoethanol (volumetric ratio of 4.5:4.5:1), followed by spin coating on Si/SiO_2 and conversion to MoS_2 via annealing at 750 and 1000°C under Ar/H_2 and Ar/S[45]. The MoS_2 channel was defined by photolithography and dry etching using O_2 plasma. The electrodes were fabricated via e-beam evaporation of Au/Ti. However, the PDs in Ref.[45] showed R_{ext} limited to$\sim 63\mu$A/W at 405nm[45] due to the presence of defects[45]. These acted as trap states and resulted in a slow (few s) τ_{life}. The current ($\sim 10^{-9}$A when the light was turned on) did not recover to the initial level ($\sim 3\times 10^{-12}$A with light off[45]). τ_{life} improved to$\sim$20ms by applying a gate pulse$\sim$100V to discharge the trapped charges[45]. Lateral heterostructures based on LPE MoS_2 flakes as photoactive material and$\sim$4 layer graphene (4LG) flakes[41, 46] or Ag paste[47] as electrodes were reported[41, 46, 47], with R_{ext} $\sim 36\mu$A/W and τ_{life} $\sim$60ms at 532nm[47], and 300mA/W under white light. Ref.[48] reported LPE MoS_2 based PDs with R_{ext} $\sim$50mA/W at 515nm and τ_{life} $\sim$5ms, using ethyl cellulose to make percolating films with conductivity$\sim 1.72\times 10^{-2}$S/m[48]. Water-based<7LG and WS_2 inks were used in Ref.[43] to make vertical heterostructures, resulting in PD arrays. However, these PDs mostly cover visible (405-532nm)[41, 43, 45–48] with R_{ext} $\leq$50mA/W, due to photocurrent loss mainly due to traps[44, 45].

Black phosphorus (BP) is a LM interesting for broad-band PDs because of its thickness dependent direct bandgap varying from$\sim$0.3eV in bulk[49] to$\sim$2eV in 1LBP[50]. Micro-mechanical cleavage (MC) has been the main approach used to make BP PDs[51–58]. Ref.[57] demonstrated PDs based on BP flakes with thickness$\sim$10nm[57] working$\sim$532-3390nm, with R_{ext} $\sim$82A/W at $3.39\mu m$ and τ_{life} $\sim$0.13ms. BP was exfoliated on Si/SiO_2. A resist layer was patterned via e-beam lithography (EBL) for metallization and evaporation of Cr/Au as contacts[57]. Ref.[54] used MC BP ($\sim$8nm thickness), EBL, and electron-beam evaporation to form arrays of metal contacts. Ref.[54] demonstrated BP-based PDs for 400-900nm, with R_{ext} $\sim 4.3\times 10^6$A/W at 400nm, $\sim 10^3$A/W at 900nm and τ_{life} $\sim$5ms. Ref.[51] used a 225nm thick BP film stacked between two SLGs as top and bottom contacts. To prevent exposure to the environment, this was encapsulated in 18nm hBN[51]. The PDs had broadband response$\sim$632-3400nm, with R_{ext} $\sim$0.15A/W at 632nm,$\sim$1.43A/W at 3400nm, and τ_{life} $\sim$1.68ns[51]. However, MC usually produces flakes<1mm[59], without thickness control (random locations of 1L to tens nm flakes)[60, 61], and lacks reproducibility in terms of amount of material, flake size, and number of layers[62–66]. Ref.[42] used LPE BP inks to print BP/CVD SLG/Si Schottky junction PDs, with R_{ext} $\sim$164mA/W at 450nm,$\sim$1.8mA/W at 1550nm, and τ_{life} $\sim$0.55ms[42]. Si/SiO_2 was patterned with EBL, followed by e-beam evaporation of Au and lift-off. The devices were further patterned to make a window to etch SiO_2. CVD SLG was then transferred, covering the Au electrode and the Si window[42]. BP was inkjet-printed on the SLG/Si Schottky junction. This process is complex and requires expensive fabrication tools (EBL and e-beam evaporator). Ref.[67] reported SLG/LPE BP PDs. Two Au electrodes were evaporated through a shadow mask on Si/SiO_2. CVD SLG

Accepted Manuscript

Fabrication	Properties					Ref.
	Spectral range(nm)	R_{ext}(A/W)	Response time(s)	NEP ($WHz^{-1/2}$)	D*(Jones)	
IP (LPE BP t∼200nm)	488-2700	337-0.048 (488-2700nm)	50×10^{-3}	1.68×10^{-10}	10^{11}	this work
IP (LPE MoS_2 t∼1.9μm)	white light	0.3	-	-	3.6×10^{10}	[46]
IP (LPE MoS_2 t∼700nm)	515	0.05 (515nm)	5×10^{-3}	-	3.2×10^{9}	[48]
IP (LPE MoS_2 t∼1.3mm)	405-980	63×10^{-6} (520nm)	20×10^{-3}	-	4.2×10^{8}	[45]
IP (LPE MoS_2 t∼50nm)	532	36×10^{-6}(532nm)	60×10^{-3}	-	-	[47]
IP (LPE WS_2 t∼100nm)	514	0.001(514nm)	-	-	-	[43]
IP (CVD MoS_2 t=1L)	405-780	0.02-0.01 (405-780nm)	1.7	-	4.8×10^{7}	[70]
IP (LPE WS_2 t∼30nm)/PHL	632	10^{-4}(632nm)	-	-	-	[71]
IP (LPE BP)/EBL	450-1550	0.164(450nm)	550×10^{-6}	-	-	[42]
EBL (MC BP t∼8nm)	640-940	4.8×10^{-3} (640nm)	4×10^{-3}	-	-	[53]
EBL (MC BP t∼10nm)	532-3390	82 (3390nm)	130×10^{-6}	5.6×10^{-12}	-	[57]
EBL (MC BP t∼10nm)	830	53(830nm)	-	-	-	[72]
EBL (MC BP t∼30nm)	400-3750	0.35×10^{-3}(1200nm)	40×10^{-6}	-	-	[68]
UVL (MC BP t∼60nm)	635-1550	594-3300(635-1550nm)	3×10^{-3}	-	-	[69]
EBL (MC BP t∼8nm)	400-900	4.3×10^{6}-10^{3}(400-900nm)	5×10^{-3}	-	-	[54]
EBL (MC BP t∼225nm)	632-3400	0.15-1.43(632-3400nm)	1.8×10^{-9}	7×10^{-12}	-	[51]
Abration (WS_2 t∼30nm)	625	144×10^{-3}(625nm)	70×10^{-6}	-	10^{8}	[182]
Sputtered (WS_2 t∼4nm)	450-635	1.68×10^{-3}(450nm)	-	-	-	[183]
EBL (WS_2 t∼7.2nm)	405-635	160×10^{-3}(405nm)	21×10^{-3}	-	1.4×10^{11}	[184]
MLL (Carbon QDs/MoS_2 t=1L)	300-700	377(360nm)	7.5	-	1.6×10^{13}	[185]
Abration (MoS_2 t=15-25μm)	365-940	1.5×10^{-6}(660nm)	20-30	-	-	[186]

TABLE I. PDs based on MC BP and LPE BP. IP (inkjet printing), EBL (e-beam lithography), PHL(photolithography), UVL (UV lithography). t: average LM film thickness.

was wet transferred on the printed LPE BP. The resulting SLG/BP film was transferred on Si/SiO_2 with Au electrodes[67]. These PDs had $R_{ext} \sim 7.7\times10^3$A/W at 360nm at 5V bias, with τ_{life} ∼7s and operation wavelength∼360-785nm[67]. Table. I compares the results of MC BP and inkjet-printed BP PDs with different device structures[42, 43, 45–48, 51, 53, 54, 57, 68–72]. To the best of our knowledge, there are no reports of inkjet-printed PDs with broadband operation from visible (∼400-700nm) to SWIR (∼2500nm), with R_{ext} >1A/W in visible and τ_{life} ∼10-50m, suitable for video imaging[73].

Printing can be used for large-scale(>1m^2)[74] fabrication of optoelectronic devices on both rigid[75] and flexible[76] substrates. A variety of printed devices have been reported[77], such as radio-frequency identification (RFID) tags on paper[78, 79], sensors[80], displays[81], memories[82], and thin-film transistors[33]. Printing was performed with a variety of methods, such as screen[83, 84], gravure[85], flexography[86], and inkjet[33, 87]. Amongst those, inkjet printing is one of the most promising, because of attractive features such as direct patterning (mask-free)[88, 89] and resolution[90, 91]. The typical printing resolution is∼100μm for gravure[92],∼100-200μm for flexo[92],∼100μm for screen printing[92]. Inkjet printing offers resolution down to∼50μm[93], which can be made<500nm by pre-patterning[94]. Inkjet printers can also be used to dispense etching[95] or patterning agents[96].

Here we use inkjet printing to fabricate SLG/BP PDs. CVD SLG is patterned via inkjet printing polyvinylpyrrolidone (PVP) as mask, followed via reactive ion etching (RIE). PVP is rinsed with water. Source-drain Ag electrodes are then inkjet-printed at the end of the SLG channel. LPE BP is inkjet-printed on the channel, followed by encapsulation using Parylene C to prevent BP oxidation[97].

Our PDs have R_{ext} up to∼337A/W at 488nm for 1V bias, the highest reported to date for inkjet-printed LPE LMs, to the best of our knowledge, see Table I. Our PDs work in the range∼488nm-2.7μm, the broadest for inkjet-printed based PDs, to the best of our knowledge, see Table I. Instead of TMDs which have tuneable indirect band gap in bulk crystals[98] and direct band gap in 1L[99], here we use BP, which exhibits thickness dependent direct bandgap from∼0.3eV in bulk[49] to∼2eV in 1LBP[50]. R_{ext} is proportional to the mobility,μ, as[6]:

$$R_{ext} = \frac{\Delta I}{P_{opt}} \frac{\tau_{life}\mu V_{ds}}{L^2} \quad (5)$$

with τ_{life} the response time, V_{ds} the bias applied between source and drain, and L the channel length. The term $\frac{\tau_{life}\mu V_{ds}}{L^2}$ is called gain[6]. By increasing μ, the gain increases, which results in higher R_{ext}. Therefore, we use CVD SLG withμ ∼1700cm^2/V.s, instead of solution-processed graphene with μ ∼300cm^2/V.s as in Ref.[100].

Accepted Manuscript

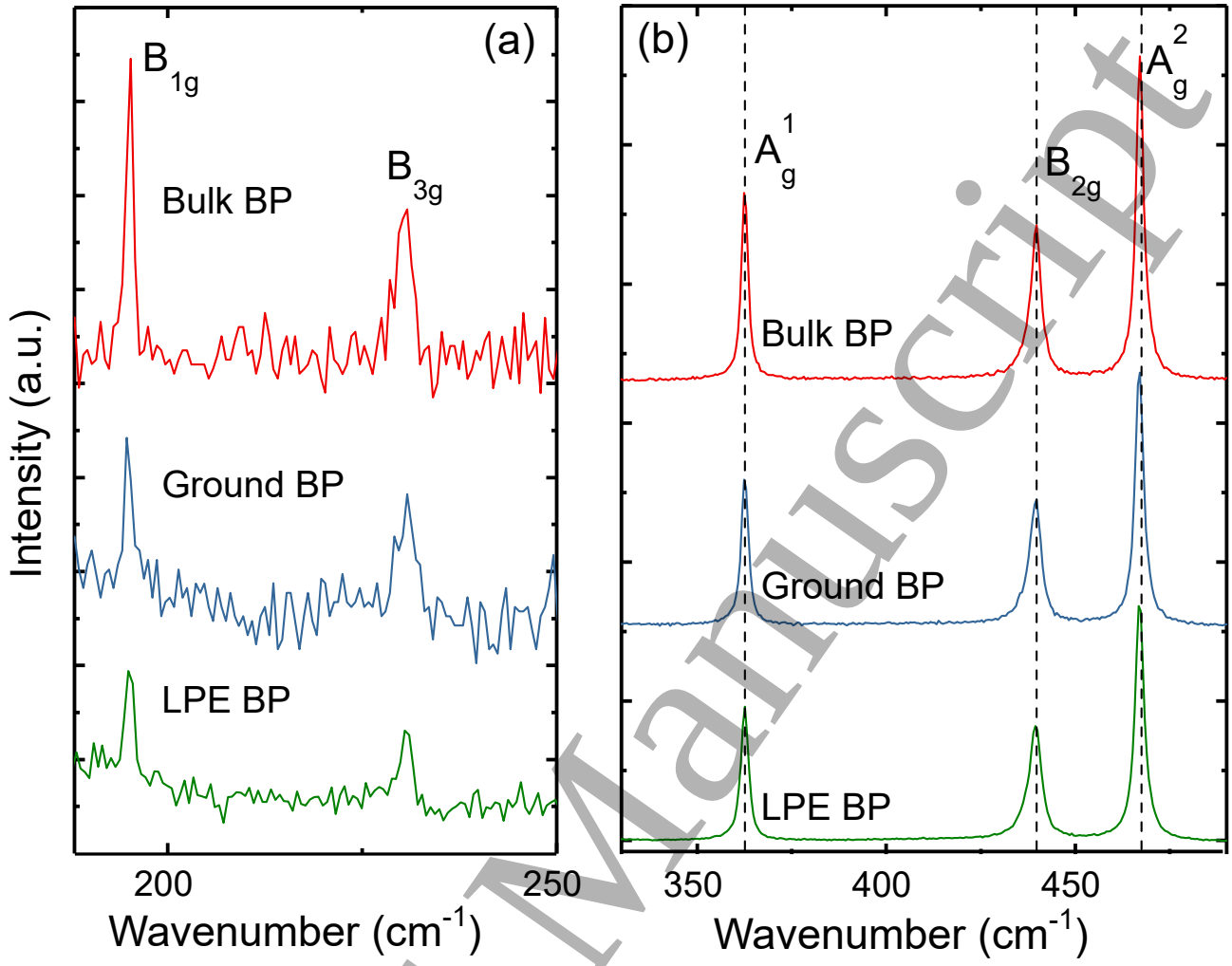

FIG. 1. (a,b) Raman spectra measured at 514.5nm of (red) BP bulk crystals, (blue) ground BP, (green) LPE BP.

To demonstrate the viability of our approach for flexible and wearable electronics, we fabricate SLG/BP PDs on polyester fabric, with R_{ext} ~6mA/W at 1V and 488nm, higher than CVD SLG PDs (R_{ext} ~0.11mA/W) on flexible (acrylic) substrates[101] and comparable to CVD MoS_2 PDs (R_{ext} ~20mA/W at 405nm) with inkjet-printed poly(3,4-ethylenedioxythiophene) polystyrene sulfonate (PEDOT:PSS) on polyethylene naphthalate (PEN)[70], but with surface roughness lower then our fabric. Thus, inkjet lithography is promising for LMs-based optoelectronic devices on textiles.

RESULTS

Inkjet printing

BP bulk crystals are sourced from Smart-elements GmbH. These are then exfoliated as follows. 15mg are transferred to a mortar and ground for~20min to facilitate subsequent sonication. BP powders are then mixed with 15ml anhydrous isopropyl alcohol (IPA) (Sigma-Aldrich) in a Schlenk flask, sealed with parafilm, and sonicated for 3h in a 900W ultrasonic bath (Fisherbrand Elmasonic S 300 Ultrasonic). The BP solution is then centrifuged (H-641 swinging bucket rotor in a Sorvall WX-100) at 4000rpm (~6000g) for 20min to let the unexfoliated flakes sediment[65, 102]. The supernatant is collected and used for characterization and printing. All procedures are carried out in a glove box (inert atmosphere to minimise BP exposure to the environment or air), except the centrifugation.

The BP crystals are characterized by Raman spectroscopy using a LabRAM HR Evolution equipped with a 100× objective with power on the sample<0.5mW to exclude heating effects, Fig.1. Bulk BP (red) has three main peaks, Fig.1b. One out-of-plane A_g^1 mode, with position Pos(A_g^1)~362.6cm^{-1}[61, 97, 103–105] and two in-plane B_{2g} and A_g^2 modes, Pos(B_{2g})~439.5 and Pos(A_g^2)~467.1cm^{-1}[61, 97, 103–105]. The cor-

Accepted Manuscript

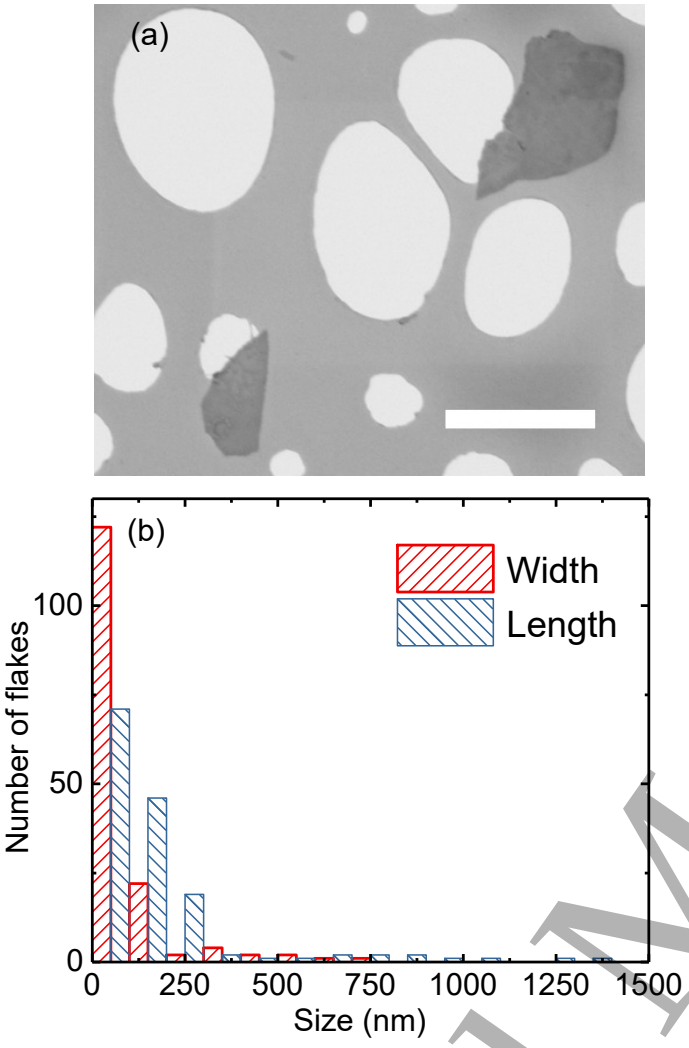

FIG. 2. (a) Representative STEM image of LPE BP. Scale bar 1μm. (b) Size statistics of 140 flakes.

responding full width at half maximum (FWHM) are FWHM(A_g^1)$\sim$2cm^{-1}, FWHM(B_{2g})$\sim$3.5cm^{-1}, FWHM(A_g^2)$\sim$2.5cm^{-1}. The peaks$\sim$194 and$\sim$230cm^{-1} are assigned to B_{1g} and B_{3g} modes[106]. These are expected to appear when the incident light has a polarization component along the axis orthogonal to the BP layers[107]. However, we detect both, although we are in backscattering, as for previous reports[106–108].

The ground BP sample (blue curve in Fig.1) has Pos(A_g^1)$\sim$362.6cm^{-1}, FWHM(A_g^1)$\sim$2.1cm^{-1}, Pos(B_{2g})$\sim$439.4cm^{-1}, FWHM(B_{2g})$\sim$3.8cm^{-1}, Pos(A_g^2)$\sim$466.9cm^{-1} with FWHM(A_g^2)$\sim$2.7cm^{-1}, Fig.1b. We observe $<$0.3cm^{-1} change in FWHM and Pos(A_g^1, B_{2g}, A_g^2) compared to bulk BP, indicating the presence of flakes with number of layers, N$>>$6[97].

The LPE BP flakes (green in Fig.1) have Pos(A_g^1)$\sim$362.6cm^{-1}, FWHM(A_g^1)$\sim$2.3cm^{-1}, Pos(B_{2g})$\sim$439.3cm^{-1}, FWHM(B_{2g})$\sim$3.9cm^{-1}, Pos(A_g^2)$\sim$466.9cm^{-1}, FWHM(A_g^2)$\sim$2.8cm^{-1}, Fig.1b.

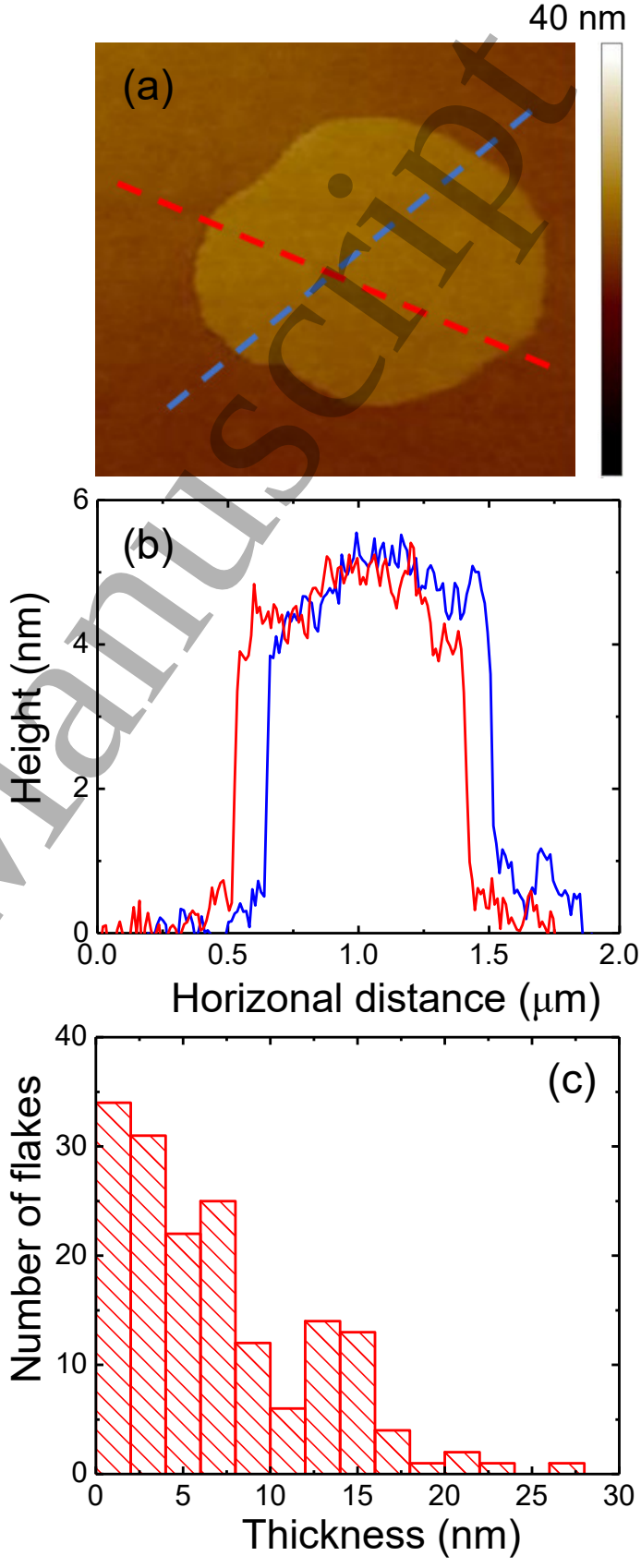

FIG. 3. (a) Representative AFM image of BP flake, and (b) height profile. (c) AFM thickness statistics of 140 flakes.

Accepted Manuscript

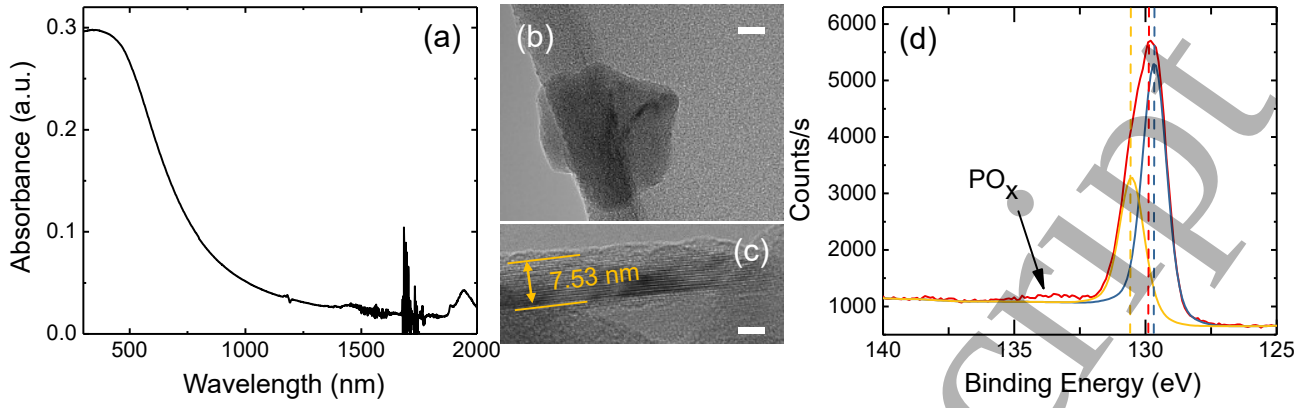

FIG. 4. (a) Absorbance of LPE BP. The ambient moisture absorbed by the IPA results in absorbance variations∼1700-1800nm[42]. The dispersions are diluted 6 times to avoid detector saturation. (b) HRTEM image of representative BP flake, scale bar 10nm. (c) Zoom of (b), scale bar 5nm. The crystal plane spacing is∼0.21nm, corresponding to the (002) plane of orthorhombic phosphorus[118]. (d) Representative XPS of LPE BP flake, showing the $2p^{3/2}$ and $2p^{1/2}$ ∼129.7[65, 119] and 130.5eV[65, 119]. Small PO_x sub-bands are seen∼134eV[119–121].

We observe <0.5cm^{-1} change in FWHM and Pos(A_g^1, B_{2g}, A_g^2) compared to bulk BP, indicating N>6[97].

Stable jetting happens when a single droplet is produced for each electrical impulse, with no secondary droplet formation[93]. This depends on ink viscosity η(mPas)[109], surface tension γ(mNm^{-1})[109], density ρ(gcm^{-3})[109] and nozzle diameter $D(\mu m)$[110]. A dimensionless figure of merit (FOM) $Z = (\gamma\rho D)^{1/2}/\eta$ was suggested to characterize the stability jetting of an ink[109, 110]. Ref.[111] reported that if Z<1 the ink would not jet, Z>14 would result in secondary droplets. Therefore, 1<Z<14 is generally considered as the optimal range for stable drop-on-demand[109, 110]. However, we previously showed that drop-on-demand inkjet printing of LM inks with Z>14 is possible[33]. By changing η, γ, and ρ we are able to tune Z across and outside the conventionally optimal range to optimize our inks for drop-on-demand printing. The size of flakes in solution should be$\sim 1/50-1/20$ smaller than the nozzle diameter to prevent clogging[33], and clustering of the particles at nozzle edge[33]. Flakes tend to concentrate at the droplet edge during evaporation, resulting in a ring-like deposit, the so-called coffee-ring effect[112], leading to printing non-uniformity[112]. Adding polymer binders into the LPE dispersion[40, 47, 113] might prevent[40] or alleviate[40] the formation of coffee-rings[40, 47, 113]. However, binders decrease electrical conductivity[40] and must be annealed for removal (e.g. baking on a hot plate at 300-400°C for∼1h[40]). Solvents like N-Methyl-2-pyrrolidone (NMP) are generally the preferred option to disperse BP because of NMP's surface tension and Hansen solubility parameters[32, 114]. However, a temperature close to the NMP boiling point (204°C)[115]) is required to remove NMP residuals[92], but this can cause oxidation[65, 97] and degradation[65, 97] of air-sensitive BP[42]. NMP is also toxic[116] and can affect the central nervous system[117], so LMs inks dispersed in NMP cannot be used in an open environment[40]. Therefore, it is better to formulate BP inks in nontoxic solvents, with boiling point<100°C.

We prepare our BP ink in anhydrous IPA (not as toxic as NMP[122], and commercially available as a 70% solution in rubbing alcohol and hand sanitizers[122]), with a boiling point∼83°C[115]. The surface tension and viscosity are characterized via contact angle, surface tension (First Ten Angstroms) and rheometery (Discovery HR-1) measurements at room temperature (RT) and ambient pressure. The BP ink has η ∼0.55mPas, γ ∼26mNm^{-1} and ρ ∼0.8gcm^{-3}. For printing we use a Fujifilm Dimatix DMP-2800 with D=22μm, resulting in Z=35, outside the conventional optimal range[111]. We aim for BP flake sizes∼1μm to prevent nozzle clogging[33]. Scanning tunneling electron microscopy (STEM) (Magellan 400L) is used to measure the flakes lateral size.

Figs.2a,b are a representative STEM image and a statistical analysis on 140 flakes, indicating mean length∼220nm and mean width∼96nm. The thickness distribution is estimated by Atomic Force Microscopy (AFM, Bruker Dimension Icon). Fig.3a is a typical AFM image of one flake, with thickness∼5.4nm, Fig.3b, corresponding to N∼11. The AFM statistics on 140 flakes shows an average thickness∼6.7nm, Fig.3c, corresponding to N∼13, given a 1L-BP thickness∼0.5nm[123].

Fig.4a plots the absorbance, Abs=-log10(Tr)[124], with Tr the transmittance of the BP ink measured with a Cary 7000 UV-VIS-NIR Spectrometer. The BP concentration is estimated from the Beer-Lambert Law[125, 126] $Abs = c \times \epsilon_{ext} \times l$, where c [gL^{-1}] is the concentration, ϵ_{ext} [Lg^{-1}m^{-1}] the extinction coefficient, and l[m] is the cuvette lenght[127]. Ref.[65] experimentally derived the BP ϵ_{ext} at 660nm from the slope of Abs per length versus the concentration of BP, ϵ_{ext} ∼267Lg^{-1}m^{-1}, with c calcu-

Accepted Manuscript

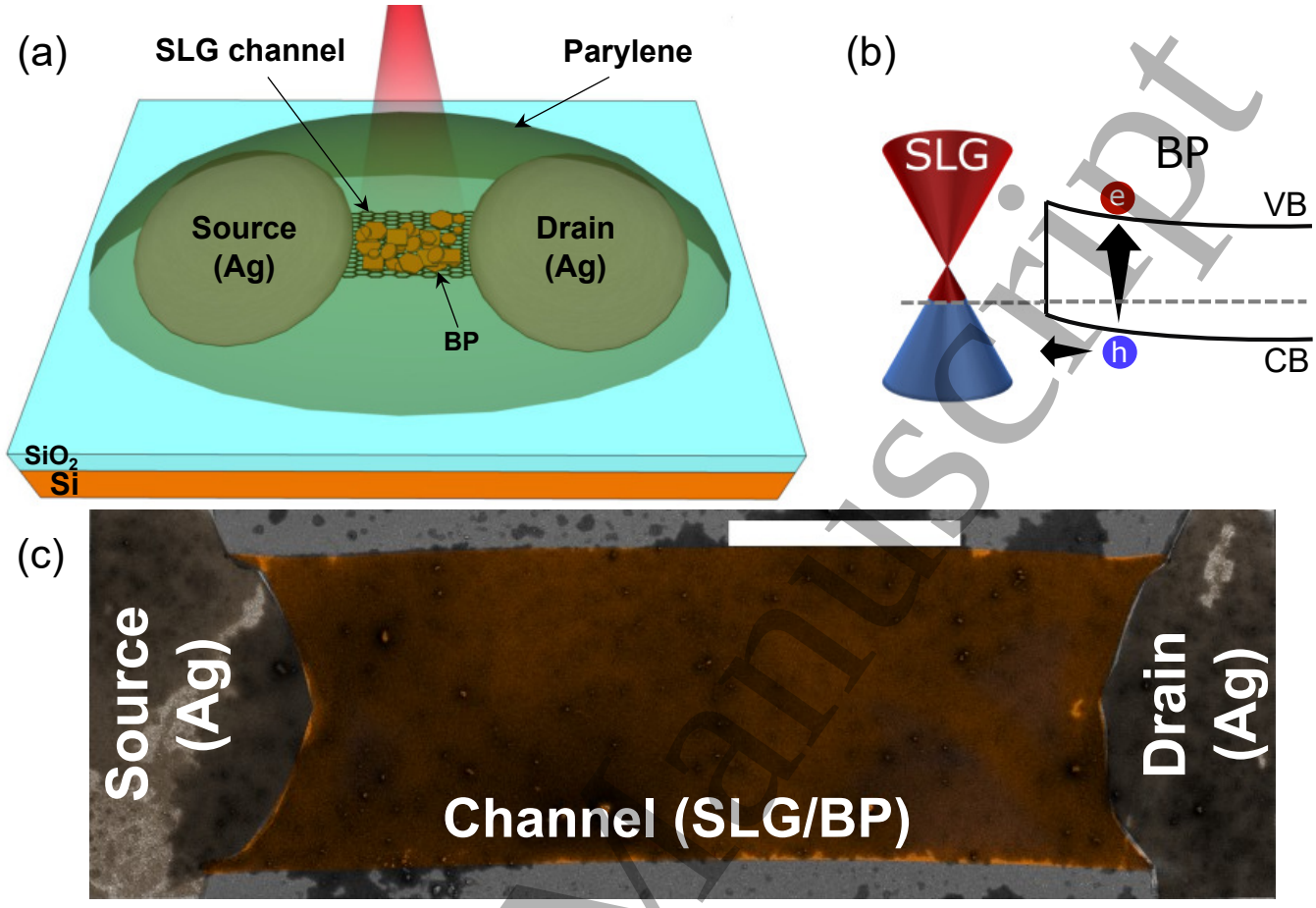

FIG. 5. (a) Schematic of SLG/BP PD. SLG is the channel (black honeycomb), BP is the photoactive material (orange), Ag is used for electrodes (silver), Parylene C as encapsulation layer (transparent green), incident light (red). (b) Schematic band diagram of SLG/BP interface, showing the BP CB and VB, generation of e/h pairs and transfer of h from BP to SLG. (c) False colour SEM image of SLG/BP PD on Si/SiO_2. BP is inkjet-printed on SLG channel (orange). Ag inkjet-printed source and drains are shown in sliver. Scale bar 15μm.

lated by measuring the weight difference of the collected BP flakes on an anodic aluminum oxide membrane before and after vacuum filtration[65]. From this, we estimate c$\sim$0.36gL^{-1} for our ink, similar to Ref.[65].

High-resolution transmission electron microscopy (HRTEM) images are obtained via a FEI Tecnai F20 FEG TEM operated at 200keV on BP flakes transferred on holey carbon grids. Figs.4b,c indicate a crystal plane spacing$\sim$0.21nm, corresponding to the (002) plane of orthorhombic phosphorus[118], with N$\sim$15, and overall thickness$\sim$7.5nm, consistent with the flake distribution range obtained by AFM in Fig.3c.

X-ray photoelectron spectroscopy (XPS) (Thermo Fisher ESCALAB 250Xi) is then performed to assess the chemical composition of the BP flakes. The samples for XPS are prepared in an Ar glove box by drop-casting the BP dispersion onto Si/SiO_2, followed by N_2 gas flushing on a hot plate (60°C) for$\sim$5min. Fig.4d shows the $2p^{3/2}$ and $2p^{1/2}$ spin–orbit split doublet$\sim$129.7[65, 119] and$\sim$130.5eV[65, 119], consistent with previous XPS measurements on bulk BP[120, 128]. The sub-bands$\sim$134eV are attributed to surface suboxides introduced during LPE, as for Refs.[65, 119].

SLG/BP on Si/SiO_2

The design of our SLG/BP PD is shown in Fig.5a. SLG is the channel on Si/SiO_2, Si is the bottom gate, SiO_2 is the dielectric, BP is the photoactive material, Ag is used for the electrodes, and Parylene C as encapsulation layer. Upon illumination, electron-hole (e-h) pairs are photogenerated in BP. Due to the band alignment (Fig.5b) h are transferred from the BP valence band (VB) into SLG, leaving behind uncompensated e, acting as an additional negative gate bias, leading to a photogating effect[12]. A schematic band diagram of the SLG/BP interface is in Fig.5b. A built-in field is formed at the SLG/BP interface. Upon BP photoexcitation, h are transferred to SLG under the built-in field, leaving e trapped in BP. Fig.5c

Accepted Manuscript

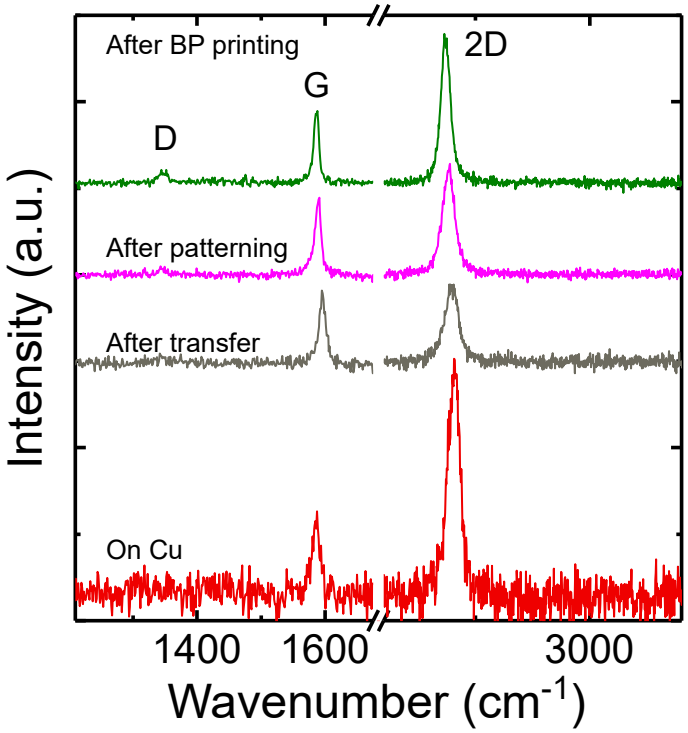

FIG. 6. Raman spectra at 514.5nm of SLG on Cu (red), after transfer (gray), after patterning and PVP removal (purple), and after BP deposition with encapsulation of parylene C and subtraction of the parylene C signal (green). Spectra normalized to have the same I(G).

is a false color SEM image of the SLG/BP PD.

To fabricate the SLG/BP PD, SLG is grown on a 35μm Cu foil, as for Ref.[130]. The substrate is annealed at 1000°C for 30min in the presence of 20sccm H_2. To initiate growth, 5sccm CH_4 is added. After growth, the sample is cooled to RT at 1mTorr.

The SLG quality is monitored at each step of the fabrication process by Raman spectroscopy. The Raman Spectrum of as grown SLG on Cu is in Fig.6, after Cu photoluminescence (PL) removal[129]. The 2D peak is a single Lorentzian with FWHM(2D)$\sim$29cm^{-1}, signature of SLG[131]. Pos(G) is$\sim$1586cm^{-1}, with FWHM(G)$\sim$14cm^{-1}. Pos(2D) is$\sim$2703cm^{-1}, I(2D)/I(G) and A(2D)/A(G) are$\sim$3.1 and $\sim$6.4. No D peak is observed, indicating negligible defects[132].

The fabrication process flow for SLG/BP PD is outlined in Fig.7. To transfer SLG, poly(methyl methacrylate) (PMMA) is spin coated on SLG/Cu, followed by oxygen etching of SLG on the Cu backside, using a RIE-NanoEtch (3W 30s). Cu/SLG/PMMA is then left in ammonium persulfate (APS) in DI water for$\sim$6h until Cu is etched. The resulting SLG/PMMA membrane is placed in DI water to clean the APS residuals and then transferred onto Si+90nm SiO_2, followed by overnight drying and PMMA removal with acetone and IPA, Fig.7a.

The Raman spectrum of SLG transferred on Si/SiO_2 is in Fig.6. The 2D peak retains its single-Lorentzian line shape with FWHM(2D)$\sim$31.6cm^{-1}. Pos(G)$\sim$1594cm^{-1}, FWHM(G)$\sim$11.6cm^{-1} and Pos(2D)$\sim$2693.1cm^{-1}, I(2D)/I(G) and A(2D)/A(G) are$\sim$1.2 and 3.2, indicating a p-doping with Fermi energy, E_F, $\sim$450meV[133, 134], which corresponds to a carrier concentration$\sim$12.3$\times$10^{12}cm^{-2}[133]. I(D)/I(G)$\sim$0.06 corresponds to a defect density of$\sim$3.54$\times$10^{10}cm^{-2}[135, 136] for excitation energy 2.41eV and E_F $\sim$450meV.

Pos(G) and Pos(2D) are also affected by the presence of strain. For uniaxial(biaxial) strain, Pos(G) shifts by ΔPos(G)/Δ ϵ_{strain} $\sim$23(60)cm^{-1}/%[137, 138]. Pos(G) also depends on doping[133, 134]. The average doping as derived from A(2D)/A(G) should correspond to Pos(G)$\sim$1599.2cm^{-1} for unstrained graphene[133]. However, in our experiment Pos(G)$\sim$1594cm^{-1}, which implies a contribution from uniaxial (biaxial) strain$\sim$0.22% (0.08%)[137]. Local variations in strain and doping manifest as a spread in Pos(G) and Pos(2D), which in our sample varies from 1592 to 1597cm^{-1} and from 2688 to 2696cm^{-1}, Fig.8a. In presence of uniaxial (biaxial) strain, and in the absence of doping, ΔPos(2D)/ΔPos(G)$\sim$2.2[137, 138]. In our samples ΔPos(2D)/ΔPos(G)$\sim$0.87 (Fig.8a), which indicates that most of the variation of Pos(G) is due to doping[137, 138]. This is also confirmed by the inverse correlation of FWHM(G) with Pos(G) in Fig.8d[133, 139, 140].

To pattern the CVD SLG, we use an IPA based PVP ink as mask, to protect SLG during RIE etching. PVP is used due its solubility in IPA[141], stable jetting[93] and ease of removal with water[142]. To make the ink, 5mg PVP (Sigma-Aldrich) is dispersed in 5ml IPA. The PVP ink has η $\sim$1.25mPas, as measured with Rheometery (Discovery HR-1), γ $\sim$69mNm^{-1}, as determined with a FTA100 series contact angle and surface tension measurement system (First Ten Angstroms) and ρ $\sim$1gcm^{-3}, as derived by weighting a known volume of PVP ink via microbalance (Sartorius). For D=22μm, Z=30. We use a Fujifilm Dimatix DMP-2800 to inkjet print PVP, while Si/SiO_2 is kept at$\sim$60°C to promote ink drying. To pattern SLG, PVP is printed on SLG to mask selected SLG regions, Fig.7b. Then, the sample is placed in a RIE to etch the uncovered SLG, Fig.7c. PVP is then removed by adding droplets of water, Fig.7d.

The Raman spectrum of etched SLG after PVP removal is in Fig.6. The 2D peak retains its single-Lorentzian shape with FWHM(2D)$\sim$33.7cm^{-1}. Pos(G)$\sim$1588.1cm^{-1}, FWHM(G)$\sim$15.6cm^{-1}, Pos(2D)$\sim$2689.6cm^{-1}, I(2D)/I(G) and A(2D)/A(G) are$\sim$1.7 and 3.8, indicating a p-doping with E_F $\sim$380meV[133, 134], corresponding to a carrier concentration$\sim$8.7$\times$10^{12}cm^{-2}[133]. I(D)/I(G)$\sim$0.08 corresponds to a defect density$\sim$4.3$\times$10^{10}cm^{-2}[135, 136] for excitation energy 2.41eV and E_F $\sim$380meV, thus no significant additional defects are induced during inkjet-

Accepted Manuscript

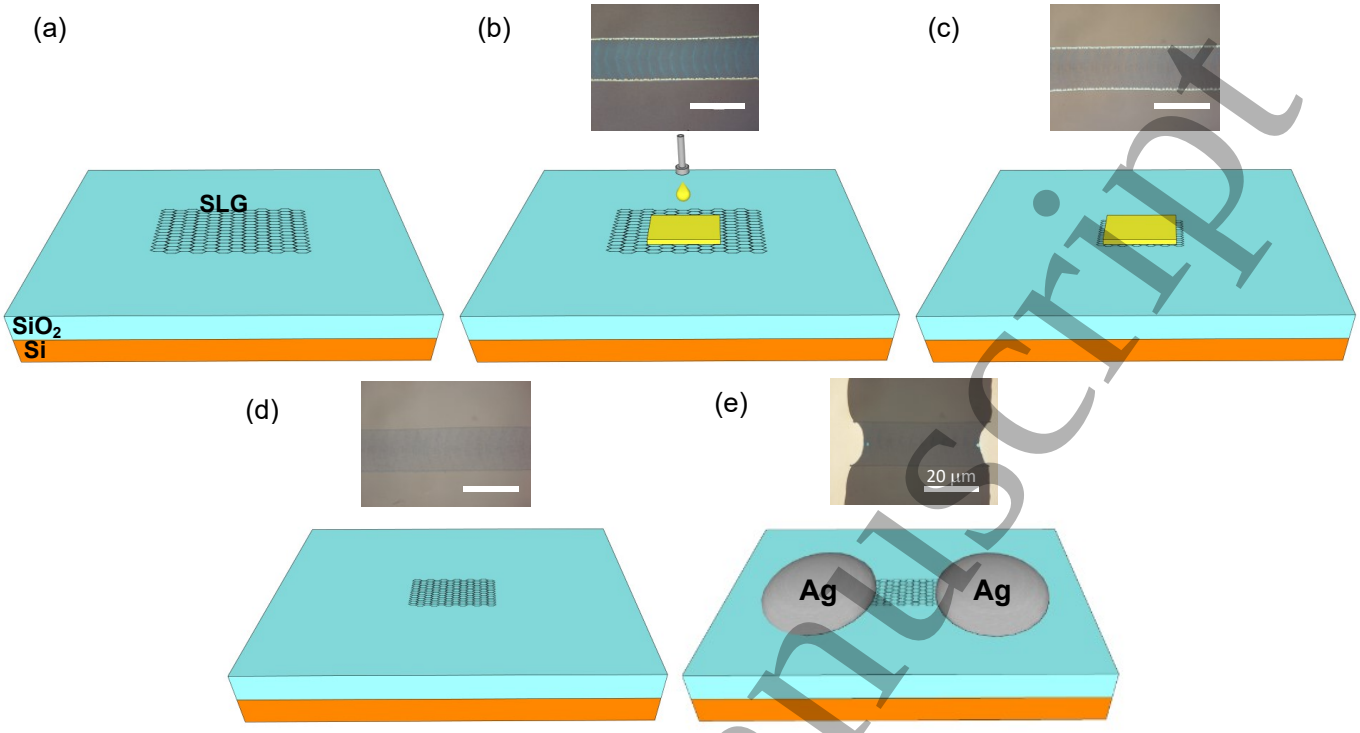

FIG. 7. Inkjet lithography of SLG-FET. (a) CVD SLG is transferred on Si/SiO_2, followed by overnight drying and PMMA removal using acetone/IPA. (b) PVP (yellow) is inkjet-printed on SLG. The optical microscopy image shows inkjed-printed PVP as mask on SLG. (c) SLG is then etched via RIE. The image shows the PVP ink on SLG after RIE etching. (d) PVP is removed by rising with water. The image shows patterned SLG after removal of PVP ink with water. (e) Ag ink (silver) is printed to make source and drain electrodes. The sample is placed on a hot plate at$\sim$150°C for$\sim$2h. The image shows the inkjet-printed Ag ink after$\sim$2h annealing. Scale bars: 20μm.

lithography. The doping estimated from A(2D)/A(G) should correspond to Pos(G)$\sim$1596.4cm^{-1} for unstrained graphene[133]. In our experiment Pos(G)$\sim$1588.1cm^{-1}, which implies a contribution from uniaxial (biaxial) strain$\sim$0.36% (0.13%)[137]. ΔPos(2D)/ΔPos(G)$\sim$0.34 (Fig.8b), which indicates that most of ΔPos(G) is due to doping[137, 138], as confirmed by the inverse correlation of FWHM(G) with Pos(G) in Fig.8e[133, 139, 140].

Source and drain electrodes are then prepared by inkjet printing an Ag ink from Sigma-Aldrich (Ag dispersion, 736465), Fig.7e, with resistivity$\sim$ 11.2$\mu\Omega$cm, as measured via a Keithley source meter at the two ends of the channel layer. The linear relation between current and source-drain voltage, V_{ds}, indicates an Ohmic contact between Ag and SLG channel, Fig.9a. The resistance of the channel is$\sim$2.07kΩ. The average sheet resistance, R_S, of CVD SLG on Si/SiO_2 measured using a 4-point probe method is $R_S \sim 600\Omega/\square$. In SLG, $R_S=(\sigma_{2d})^{-1}$[27], with σ_{2d} the SLG conductivity. In SLG, $\sigma_{2d}=n\mu q$[143] where n is the carrier density per unit area and q is the e charge. From n$\sim$8.7$\times$10^{12}cm^{-2} derived from our Raman measurements, we get $R_S \sim 450\Omega/\square$, consistent with our R_S measurements.

We then gate modulate the current between SLG source and drain. SLG shows ambipolar behavior with $\mu \sim 1700 cm^2 V^{-1} s^{-1}$, Fig.9b, from Ref.[6]:

$$\mu = \frac{\triangle I_d . L}{\triangle V_g . C_{ox} . V_{ds} . W} \quad (6)$$

where $\triangle I_d$ is the change in drain current, $\triangle V_g$ is the change in gate voltage, L is the channel length, W is the channel width, and V_{ds} is source-drain voltage. C_{ox} is the gate oxide capacitance=$\epsilon_0 \epsilon / t_{ox}$, where $\epsilon_0 \sim 8.85 \times 10^{-14}$F/cm is the vacuum permittivity, $\epsilon \sim 3.9$ is the dielectric constant of SiO_2[6] and $t_{ox} \sim$90nm is the SiO_2 thickness. We use 90nm SiO_2 in order to have a larger electric field at lower gate voltages. The SLG quantum capacitance (C_Q) can be calculated as[133, 144]:

$$C_Q \sim \frac{2q^2}{\hbar v_f \sqrt{\pi}} \sqrt{p_{ch} + n_i} \quad (7)$$

Where $\hbar$ is the reduced Planck constant, $v_f = 1.1 \times 10^6 m/s$ is the SLG Fermi velocity[60, 145], p_{ch} is the charge carrier concentration per unit area in the channel, and n_i is the intrinsic carrier concentration in SLG near the Dirac point induced by defects and impurities[144, 146–148]. From the Raman analysis we estimate $n_i \sim 8.7 \times 10^{12} cm^{-2}$. This gives

Accepted Manuscript

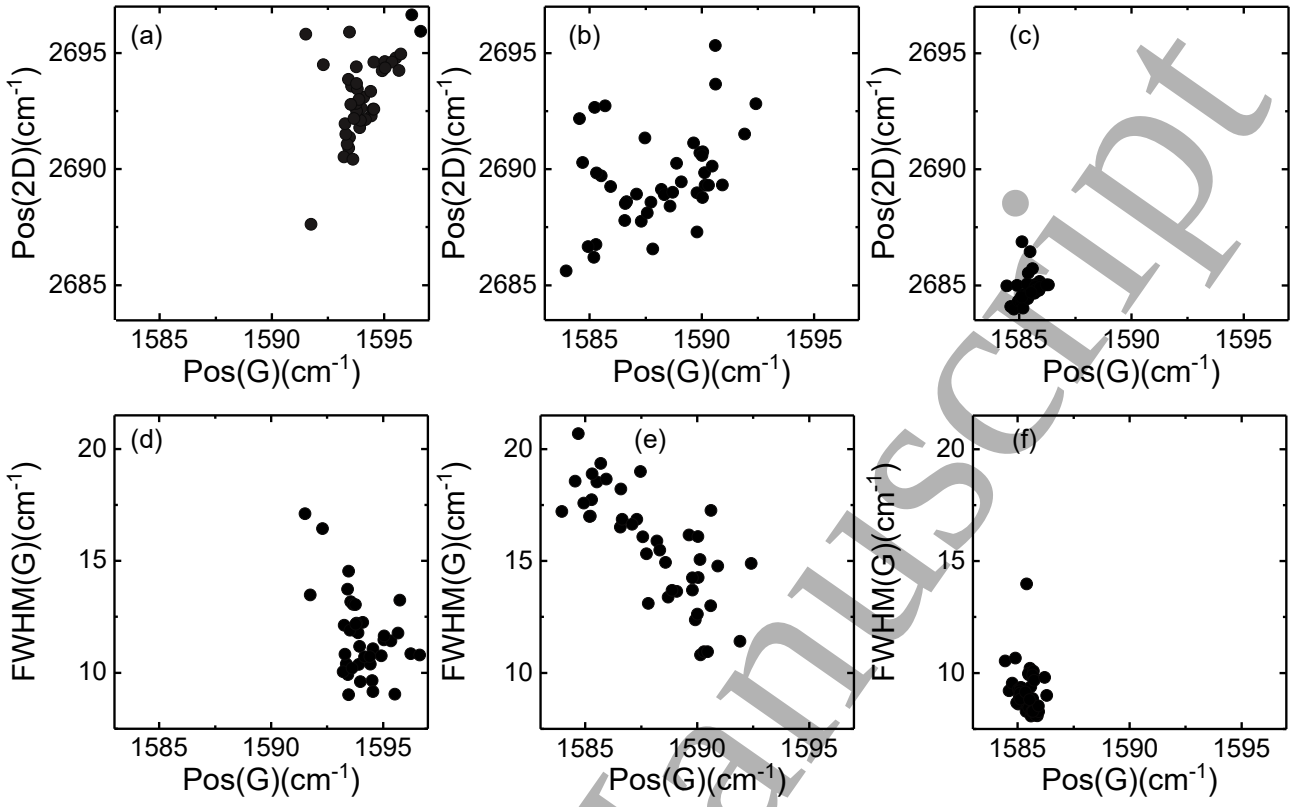

FIG. 8. Pos(2D) as a function of Pos(G) mapped across a 20μm$\times 20\mu$m region in SLG (a) after transfer, (b) after patterning and PVP removal, and (c) BP deposition. FWHM(G) as a function of Pos(G) mapped across a 20μm$\times 20\mu$m region in SLG (d) after transfer, (e) after patterning and PVP removal, and (f) BP deposition.

$C_Q \sim 6\times 10^{-6} F/cm^2$. Thus, the total capacitance $C_{Tot}=(1/C_{ox}+1/C_Q)^{-1} \sim C_{ox}$.

The contact resistance (R_c) of the Ag printed ink on SLG is estimated from the transfer length method (TLM)[6], making 6 samples of Ag/SLG/Ag contacts at SLG channel lengths$\sim$60, 160, 175, 300, 305, 430μm, Fig.9c. R_c of the Ag printed ink on SLG is$\sim$11K$\Omega.\mu$m (Fig.9c). From the linear relation between current and voltage in Fig.9c, we derive an Ohmic contact between Ag and SLG for all 6 samples.

The BP ink is then printed to a thickness$\sim$200nm to cover the whole SLG channel, as measured with a DektakXT Stylus Profilometer. To prevent BP oxidation and degradation during electrical and photodetection characterizations, the SLG/BP PD is sealed under vacuum using Parylene C dimers (Curtiss-Wright) with a parylene coater (SCS coating). This forms a barrier to moisture and gas permeability[149, 150]. Refs.[42, 97] encapsulated BP flakes with parylene C to prevent BP degradation. Following encapsulation, our SLG/BP PDs are stable for >30 days under ambient conditions. Parylene dimers are vaporized at$\sim$ 80°C. In a separate chamber, they are pyrolysed into monomers at$\sim$ 690°C. The PD is held at RT so that parylene polymerizes on contact with the surface, forming a conformal film[42].

The Raman spectra of SLG coated with BP and sealed with Parylene C are in Fig.6 after subtraction of the parylene C signal, Figs.10(a,b,c). In the Raman spectrum of Parylene C, the peaks$\sim$1207, 1337, 1610cm^{-1}, Fig.10b, are attributed to CH in-plane vibrations[151, 152], CH_2 wagging and twisting vibrations[151, 152], and CH scissoring in CH_2 and/or C-C skeletal in-plane vibrations of the aromatic ring[151, 152], respectively. The 2D peak retains its single-Lorentzian line shape, and narrows from FWHM(2D)$\sim$33.7cm^{-1} to FWHM(2D)$\sim$23.6cm^{-1}, Fig.6, 10c. FWHM(G) narrows from$\sim$15.6cm^{-1} to$\sim$9.2cm^{-1}, Fig.6, 10b. FWHM(2D) and FWHM(G) narrow due to the homogeneous distribution of doping in SLG channel. Pos(G) is$\sim$1585.4cm^{-1}, Pos(2D)$\sim$2684.8cm^{-1}, I(2D)/I(G) and A(2D)/A(G) are$\sim$2 and 5.3, indicating a n-doping with E_F $\sim$360meV[133, 134] which corresponds to carrier concentration$\sim 7.7\times 10^{12}$ cm^{-2}[133]. I(D)/I(G)$\sim$0.25 corresponds to a defect density$\sim 13.0\times 10^{10}$ cm^{-2}[135, 136] for excitation energy 2.41eV and E_F $\sim$360meV. E_F, as calculated from A(2D)/A(G), should correspond to Pos(G)$\sim$1590.2cm^{-1} for unstrained graphene[133]. We have Pos(G)$\sim$1585.4cm^{-1}, which implies a contribution from uniaxial (biaxial) strain$\sim$0.21% (0.08%)[137]. ΔPos(2D)/ΔPos(G)$\sim$0.38 (Fig.8c), which indicates that

Accepted Manuscript

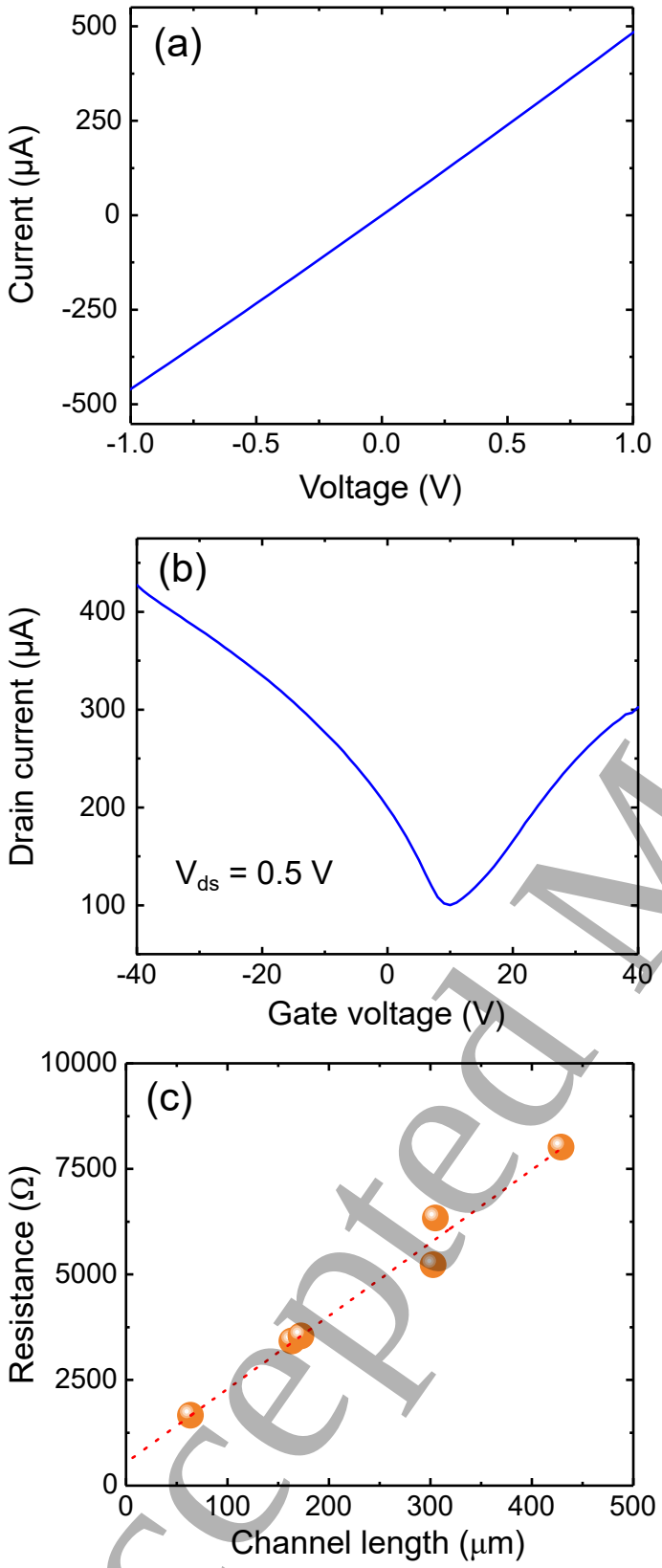

FIG. 9. (a) Current as a function of V_{ds}. (b) I_d as a function of V_g for V_{ds}=0.5V. (c) Contact resistance of inkjet-printed Ag ink on CVD SLG. The dotted line is a fit to the data.

most of the variation of Pos(G) is due to doping[137, 138]. This is also confirmed by the inverse correlation of FWHM(G) with Pos(G) in Fig.8f[133, 139, 140].

Since device fabrication comprises many steps, monitoring the quality of graphene is essential since it could affect the SLG mobility. The Raman analysis provides information on doping, defects, and strain, which affect μ, thus R_{ext}, as for Eq.5. Both compressive and tensile strains can affect μ[153]. Ref.[153] reported that a change in strain$\sim$0.012% in CVD SLG resulted in a$\sim$3 times decrease of μ. Our Raman analysis shows a change of strain$\sim$0.01% from transferred SLG on Si/SiO_2 to patterned and BP coated SLG. Thus, we expect μ to decrease$\sim$1-3 times SLG on Si/SiO_2 to patterned and BP coated SLG. This is consistent with field-effect measurements, giving μ $\sim$1200cm^2/V.s for SLG on Si/SiO_2, reduced to$\sim$650cm^2/V.s for patterned and BP coated SLG.

Fig.11a plots the drain current (I_d) as function of back gate voltages (V_g) under different optical powers, ranging from$\sim$612μW to 620nW. We do not observe light sensitivity<620nW, due to no photocurrent generation (photocurrent generation in our SLG/BP PD requires absorption and generation of e-h pairs in BP as photoactive material). Following illumination, V_D shifts to higher V_g, and I_d increases for $V_g < V_D$, where carrier transport is h dominated. Therefore, h transfer from BP to SLG is further promoted by gating. Under illumination, light is absorbed by BP and part of the photogenerated h are transferred from the BP VB into lower energy states in SLG, leaving behind uncompensated photogenerated e[69]. The latter are trapped in BP and act as an additional negative gate on the SLG channel, altering the electric field at the SLG/BP junction[69]. Fig.11b plots the photocurrent as a function of V_{ds}, defined as[6]:

$$I_{photo} = I_{light} - I_{dark} \tag{8}$$

where I_{light} is the current under illumination and I_{dark} is that in dark conditions. To derive R_{ext}, we measure I_{photo} for powers from$\sim$490 to 1.1μW, Fig.11c.

Fig.11c gives R_{ext} $\sim$337A/W for 488nm when V_g=-20V ($V_g < V_D$) and V_{ds}=1V. For V_{ds} >1V, the free carriers drift velocity $\nu_d = \frac{\mu E}{1+\mu E/\nu_{sat}}$[154], with ν_{sat} the saturation velocity of the carriers in the SLG channel and E the applied electric field to SLG, increases linearly, until saturation, due to carrier scattering with optical phonons[155]. Therefore, all measurements are done at $V_{ds} \leq 1V$ to keep the device operation in the linear (Ohmic) regime, thus eliminating the nonlinear dependence of ν_d on V_{ds}. Fig.11c shows that R_{ext} saturates for incident optical power<1μW. For P_{opt} $\sim$1.1μW the number of photogenerated carriers decreases, resulting in an increases of the built-in field at the SLG/BP interface[12, 69], which explains the enhancement of R_{ext} at lower optical powers[12, 69].

Fig.12 plots the spectral R_{ext} for SLG/BP PDs. These

Accepted Manuscript

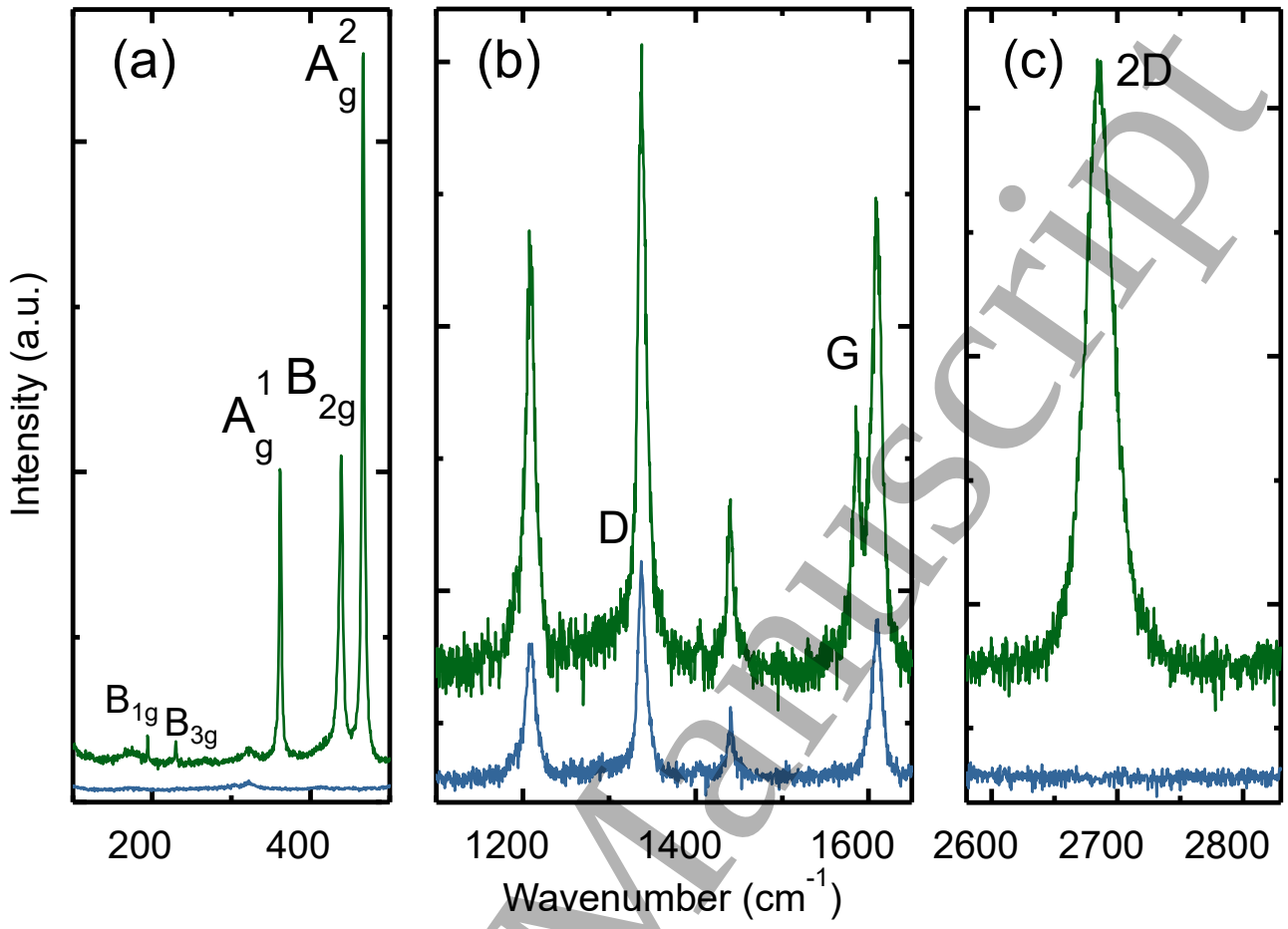

FIG. 10. Raman spectra at 514.5nm of parylene C (blue) on Si/SiO_2 and SLG/BP sealed with parylene C (green) on Si/SiO_2

show broadband R_{ext} from visible (488nm,~300A/W) to mid-infrared (2700nm,~48mA/W) at 1V.

Metal-SLG-metal PDs were reported with R_{ext} of few mA/W at 633nm[156] and 1550nm[157]. The difference in R_{ext} between these and our SLG/BP PDs is attributed to the contribution of the BP photoactive layer. To get a better understanding of spectral response versus wavelength, we perform optical simulations. We extract the BP refractive index from the solution absorbance of LPE BP, Fig.4a. Specifically, transmission in solution can be defined either by the absorbance ($Abs=c\times\epsilon_{ext}\times l$ as $T_r=10^{-c\epsilon_{ext}l}$) or by the optical depth as e^{-al}[158, 159], where l is the cuvette length and $a=a_{BP}c/\rho$, $a_{BP}=4\pi K_{BP}/\lambda$ is the BP bulk absorption coefficient, K_{BP} is the imaginary part of the BP refractive index, ρ is the BP density (2340 gL^{-1}[160]), and λ is the incident wavelength. We assume the BP flakes randomly oriented, thus seek to extract the average refractive index[161]. Then, $K_{BP}=\epsilon_{ext}\lambda\rho/4\pi\log_{10}(e)$ and the real part of the average refractive index is found by applying the Kramers-Kronig (KK) relation[161], $n_{BP}(w)=1+2\pi^{-1}\,\mathcal{P}\int_0^\infty w'\,K_{BP}(w')/(w'^2-w^2)\,dw'$, where $\mathcal{P}$ denotes the principal value of the integral and w is angular frequency. The absorbance data of Fig.4a are truncated at UV=300nm, due to the cuvette absorbance~300nm[162], making our n_{BP} extraction qualitative, because of the finite integration range. We use the extracted BP refractive index in Fresnel equation calculations[163] to estimate the absorption of SLG/BP on Si/SiO_2. The SLG refractive index is modelled by the Kubo conductance[164] at RT and E_F=0.38eV as estimated by the Raman measurements in Fig.6. Due to the fluctuations in absorbance beyond 1700nm, Fig.4a, we do not extract refractive index for BP beyond 1700nm. The experimental absorption of inkjet-printed BP/SLG on quartz is plotted in Fig.12. This follows the experimental and theoretical absorption spectra of SLG/BP films, i.e. drop of both R_{ext} and absorption with increasing wavelength, indicating R_{ext} follows the absorption spectra of the light absorbing photoactive material.

The temporal response of our PDs is then measured with a MSO9404A Mixed Signal Oscilloscope, Fig.13a. The time response in Fig.13a reaches saturation at~3.8μA, as shown by the horizontal dashed line. We thus fit the temporal response decay in Fig.13a with[73]: $I(t)=A_0.\exp(-t/\tau_{life})+B$, where A_0 is the initial cur-

Accepted Manuscript

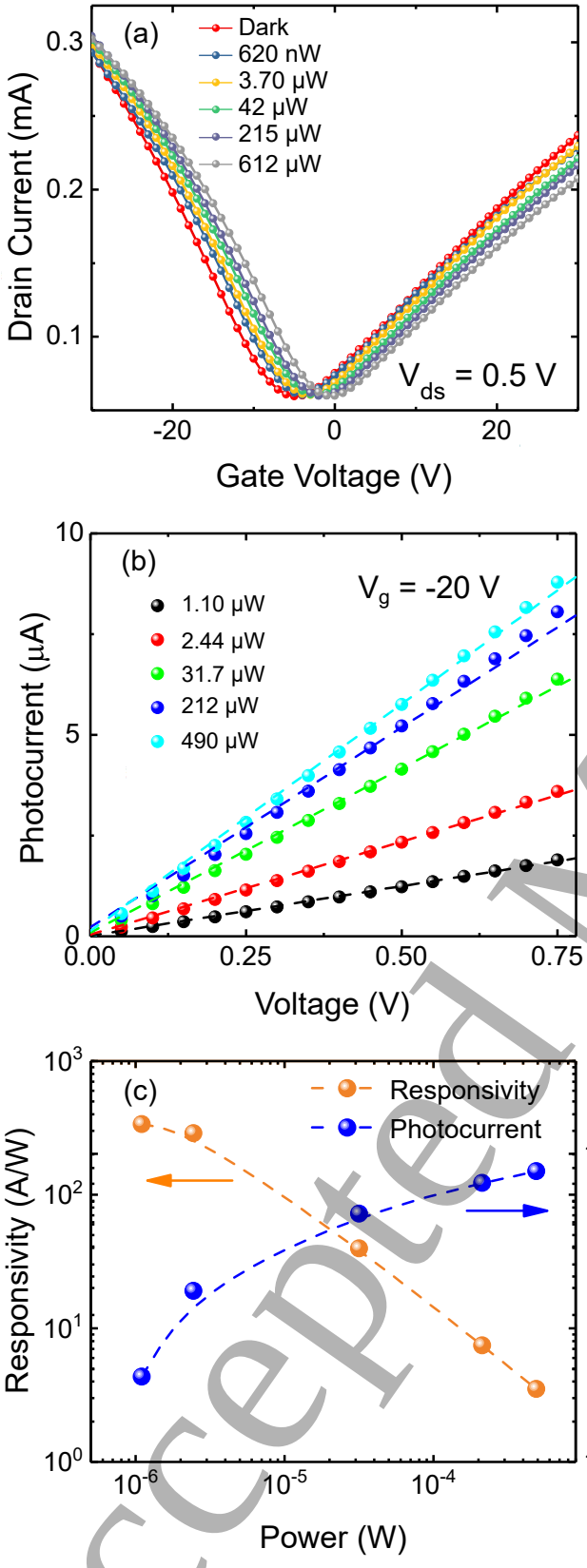

FIG. 11. (a) Gating response in dark and at 488nm from 620nW to 612μW for V_{ds}=0.5V. (b) I_{photo} at 488nm from 1.1 to 490μW. (c) R_{ext} and I_{photo} as a function of incident power.

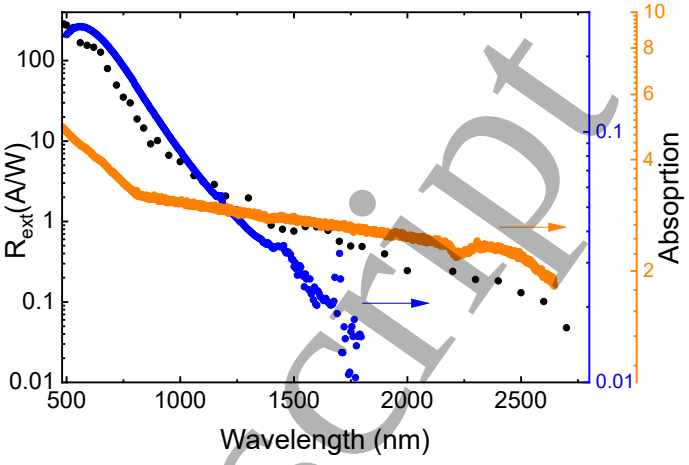

FIG. 12. Spectral R_{ext} of SLG/BP PDs (black circles), experimental absorption of SLG/BP on quartz (orange circles), and theoretical absorption of SLG/BP on Si/SiO_2 (blue circles) using the BP refractive index extracted from the absorbance of LPE BP with the KK relations[161], as a function of excitation wavelength.

rent, τ_{life} is the response time and B a constant. We get a response time∼50ms, two order of magnitudes faster than the LPE BP/CVD SLG PD of Ref.[67], consistent with other LPE based PDs[45, 165], but two orders of magnitude slower than the Schottky junction PDs of Ref.[42], which has lower R_{ext} ∼164mA/W at 450nm, due to lack of photoconductive gain, but faster response time∼550μs, because of the Schottky diode characteristics at the Si/SLG/BP interfaces[42].

By applying V_{ds}, transferred photogenerated h drift to the drain with a timescale $\tau_{transit}$[6]:

$$\tau_{transit} = \frac{L^2}{\mu V_{ds}} \tag{9}$$

where L=60μm is the length of channel, and μ ∼1700cm^{2}V^{-1}s^{-1}. We thus get $\tau_{transit}$ ∼37ns, resulting in a photoconductive gain[6]:

$$Gain = \frac{\tau_{life}}{\tau_{transit}} \sim 10^6 \tag{10}$$

The dependence of R_{ext} on $\frac{\tau_{life}}{\tau_{transit}}$ explains the decrease in R_{ext} when the optical power increases. The decrease in R_{ext} suggests an increase of $\tau_{transit}$ and/or decrease of τ_{life}. The increase of $\tau_{transit}$ is likely due to increase in scattering of photogenerated carriers in the channel with increase in optical power[166]. Auger recombination induced by increasing power can also increase the photogenerated charges recombination rate, reducing τ_{life}[166]. The gain can be further defined as the ratio of photogenerated currents recirculating in the SLG channel to the injected h from BP to SLG[69]:

$$Gain = \frac{|I_{light} - I_{dark}|}{q.A_{PD}.\triangle p_{ch}} \tag{11}$$

Accepted Manuscript

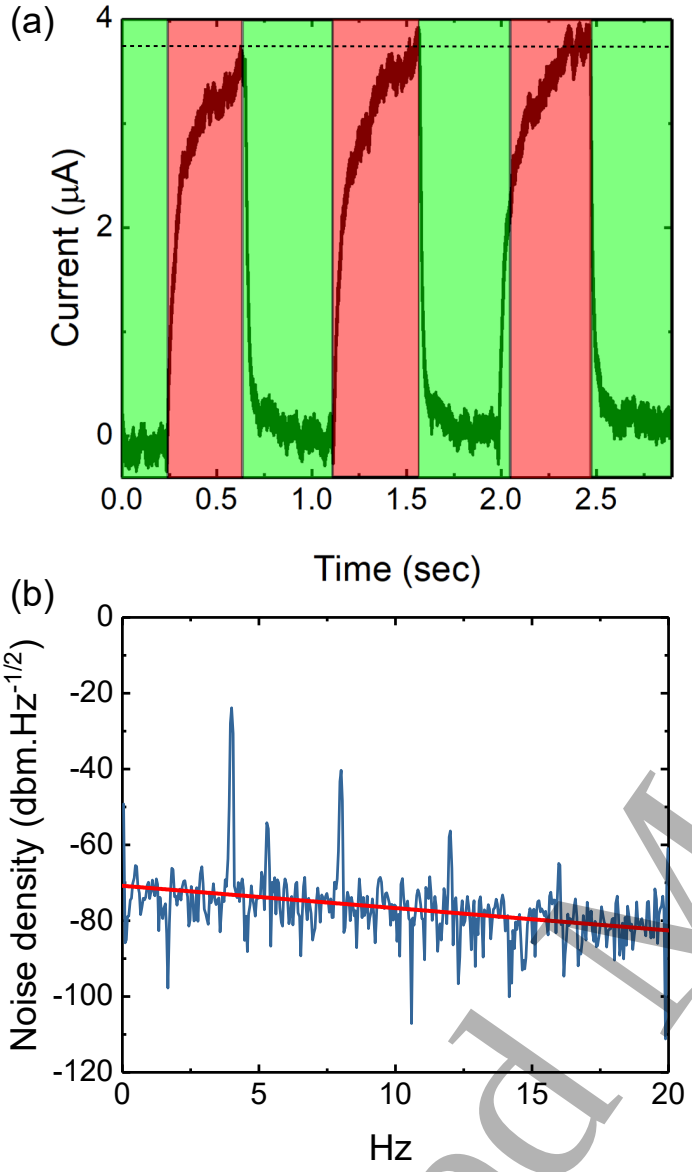

FIG. 13. (a) Time response at 642nm. The green zones indicate light off (dark condition), the red zone, light on. (b) Noise spectral density.

Where $\triangle p_{ch}$ is the concentration per unit area and per unit time of the injected h. $\triangle p_{ch}$ is equal to the trapped e concentration per unit area and per unit time in BP, related to a charge neutrality point shift $\triangle V_g = \triangle V_D$ in the transfer characteristics (I_d versus V_g). To calculate $\triangle p_{ch}$, we consider the potential balance in the metal-dielectric-SLG structure. V_g creates a potential drop ($V_{ch} = E_f/q$) so that[6, 133]:

$$V_g = V_{ch} + V_{diel} = \frac{E_f}{q} + \frac{Q_G}{C_{ox}} \quad (12)$$

where Q_G is the charge concentration. $|Q_G| = |q.p_{ch}|$ where p_{ch} is the charge carrier concentration per unit area in the channel induced by V_g. Any variation in p_{ch} changes Q_g and V_g. The derivative of V_g with respect to Q_g gives:

$$\frac{dV_g}{dQ_g} = \frac{1}{C_{ox}} + \frac{dV_{ch}}{dQ_g} \quad (13)$$

which results in:

$$\triangle Q_g = \left(\frac{1}{C_{ox}} + \frac{1}{C_Q}\right)^{-1} .\triangle V_g \quad (14)$$

To find Q_G and $\triangle p_{ch}$, C_{ox} and C_Q are needed. $C_{ox} \sim 38.35 \times 10^{-9} F/cm^2$. From Eq.7, we get $C_Q \sim 6\times10^{-6} F/cm^2$. Therefore, $\triangle p_{ch}$ varies from$\sim 2.6\times10^{11} cm^{-2}$ to $1.1\times10^{12} cm^{-2}$ for optical power 620nW to 612μW at $V_{ds} = 0.5V$. Then, from Eq.11, we get Gain$\sim 2 \times 10^6$, in agreement with Eq.10.

We then evaluate the detectivity (D^*) [$cm.Hz^{1/2}/W$ or Jones]. This relates the performance of PDs in terms of R_{ext} to A_{PD}, allowing the comparison of PDs with different A_{PD}[6]:

$$D^* = \frac{(A_{PD}B)^{1/2}}{NEP} \quad (15)$$

where B is the electrical bandwidth(Hz), defined as difference between the upper and lower frequencies of R_{ext}, and NEP is the noise equivalent power (i.e. the power that gives a signal to noise ratio of one in a 1Hz output bandwidth[6, 167]):

$$NEP = \frac{i_n}{R_{ext}} \quad (16)$$

where i_n is the dark noise current, i.e. the current that exists when no light is incident on the PD[6]. The noise [$A/\sqrt{Hz}$] is measured in the time domain, by collecting the trace on an oscilloscope, with subsequent Fourier transform in order to analyze the data in the spectral domain. Fig.13b plots the 1/f noise (where f is the frequency). 1/f is the noise density (noise power per unit of bandwidth [dBm.Hz$^{-1/2}$][6]), due to charge traps and defects[6]. At 4Hz,$\sim$5 times less than the cut off f, i.e. the f at which the detector R_{ext} decreases by 3dB[6], we get NEP$\sim 1.8 \times 10^{-10} WHz^{-1/2}$ and D* $\sim 2\times10^7$Jones. The noise current in the shot noise limit (due to generation-recombination of e-h pairs and resistive current paths in PDs[6]) is defined as $i_n = (2qI_{dark})^{1/2}$[167]. Thus, in the shot noise limit, we can write D^* as[6]:

$$D^* = \frac{R_{ext}(AB)^{1/2}}{(2qI_{dark})^{1/2}} \quad (17)$$

Eq.17 gives $D^* \sim 10^{11}$ Jones,$\sim$3 times higher than Ref.[46] for inkjet-printed graphene/MoS_2 PDs. It is also$\sim$3-4 orders of magnitude higher than Refs.[45, 48] for PDs based on inkjet-printed MoS_2. Thus, our inkjet-printed PDs are suitable for detecting weak light intensities which compete with the detector noise[6].

Accepted Manuscript

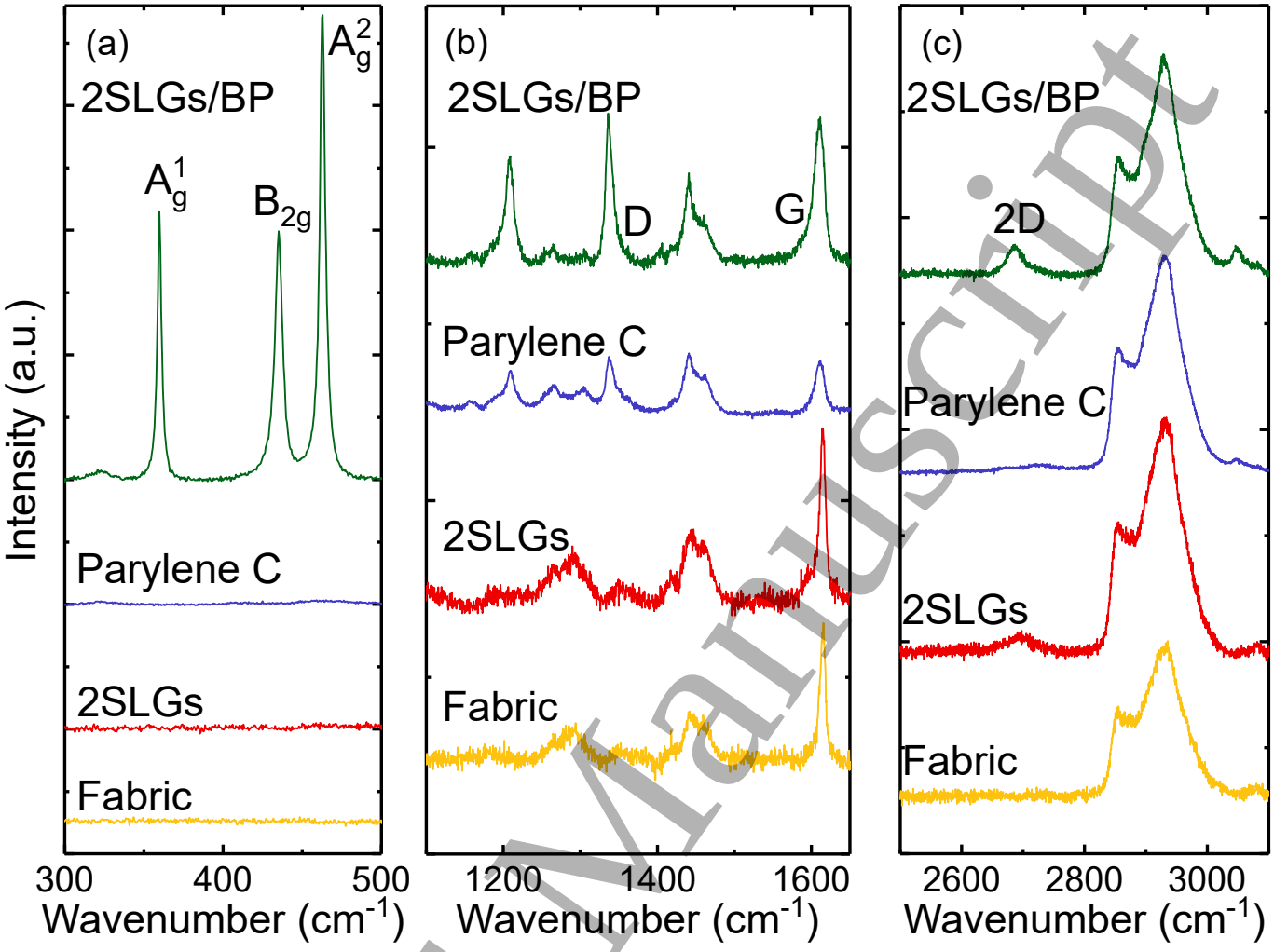

FIG. 14. (a,b,c) Raman spectra at 514.5nm of fabric (amber), 2 SLGs on fabric after patterning and PVP removal(red), parylene C on fabric (blue), and 2 SLGs/BP with encapsulation of parylene C (green).

SLG/BP on fabric

In wearable applications, inkjet lithography has advantages over EBL and other lithography techniques for patterning and device fabrications because of textiles' porous[168], rough[168] and non-conductive structure[168], which makes these lithography techniques not suitable. To showcase this, we fabricate PDs on polyester fabric, because of its durability against sun exposure[169], wrinkling[169] and shrinking[170], and common use (~52% of the synthetic textile market in 2018[168, 171]). Since the surface roughness of textiles affects the electrical conductivity[172, 173], we planarize the surface by reducing the roughness. To do so, we rod coat polyurethane (PU) 10 times to reduce the root mean square (RMS) roughness from~$50\mu m$ to $< 5\mu m$. We then transfer SLG on PU coated polyester fabric using a similar procedure as for Si/SiO_2. After removing PMMA, a PVP ink is inkjet-printed as mask on SLG to pattern a $400\mu m \times 400\mu m$ channel. SLG is then etched via RIE, followed by removal of PVP with water.

Fig.14 shows the Raman spectra of 2 SLG on PU coated polyester fabric. The PU coated polyester fabric has two bands~2935 and ~2845cm^{-1} attributed to asymmetric and symmetric C-H stretching vibrations of CH_2 groups[174, 175], Fig.14c. The peak~1615cm^{-1} can be ascribed to -C=C- stretching vibrations of aromatic rings[176, 177], Fig.14b. The peak~1442cm^{-1} can be ascribed to C-H deformation vibrations of CH_2 groups[174, 177] and that~1251cm^{-1} to coupled C-N and C-O vibrations of urethane[174, 177], Fig.14b. The spectrum of SLG on fabric has Pos(G)~1596.9cm^{-1}, FWHM(G)~14.4cm^{-1}, Fig.14b, Pos(2D)~2693.3cm^{-1}, FWHM(2D)~56.6cm^{-1}, Fig.14c. I(2D)/I(G) and A(2D)/A(G) are~1.5 and 5.8, indicating a p-doping of E_F ~270meV[133, 134] which corresponds to a carrier concentration~4.33×10^{12} cm^{-2}[133]. I(D)/I(G)~1.03 corresponds to defect density ~$4.6\times10^{11}cm^{-2}$[135, 136]

Accepted Manuscript

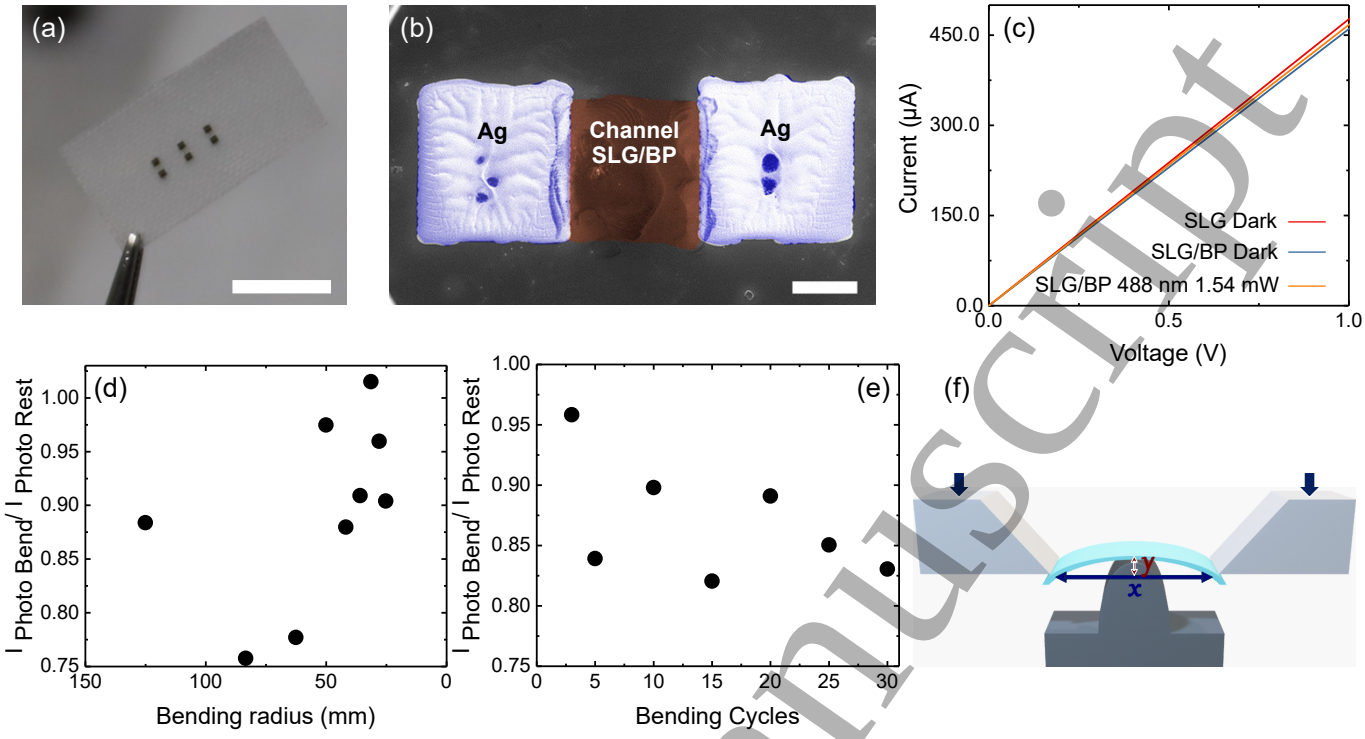

FIG. 15. (a) SLG/BP PD array on polyester fabric. Scale bar 5mm. (b) SEM of PD on polyester fabric. Scale bar 200μm. (c) Current as function of V_{ds} for SLG and SLG/BP in dark, and SLG/BP under illumination at 488nm for $\leq 1V$. (d) I_{photo} normalized to that measured on flat PD, as a function of bending radius. (e) I_{photo} normalized to that on flat PD as a function of bending cycle. (f) Schematic of bending setup. Arrows indicate applied force on grips, the bent SLG/BP PD is drawn in mint green between the grips, y is the height at the chord midpoint, and x is the chord circumference.

for excitation energy 2.41eV and E_F=270meV. For the E_F derived from A(2D)/A(G), Pos(G) should be$\sim$1589.2cm^{-1} for unstrained graphene[133]. In our experiment Pos(G)$\sim$1596.9cm^{-1}, which implies a contribution from uniaxial (biaxial) strain$\sim$0.33% (0.12%)[137], which is comparable to the uniaxial (biaxial) strain$\sim$0.36% (0.13%) of SLG on Si/SiO_2.

We then inkjet print electrodes with the Ag ink. The sample is annealed at$\sim$100°C for$\sim$2h to remove residual solvent (triethylene glycol monomethyl ether). We transfer two SLG to have R_s $\sim$2.1KΩ, comparable to transferred CVD SLG previously reported for polypropylene coated fabrics[173]. BP is then inkjet-printed on the channel layer. Figs.15a,b are optical and SEM images of PDs on polyester fabric. Fig.15c plots the current-voltage characteristic in dark, which shows an Ohmic resistance ($R = 2.09K\Omega$) between inkjet-printed electrodes and SLG channel. We then characterize R_{ext} at 488nm for P=1.1mW. Fig.15c shows that the current increases under illumination and we get R_{ext} $\sim$6mA/W at 488nm.

The Raman spectrum of BP coated on SLG on fabric is in Fig.14a. Pos(G)$\sim$1587.4cm^{-1}, FWHM(G) broadens from $\sim$14.4cm^{-1} to$\sim$15.6cm^{-1}, Fig.14b, Pos(2D)$\sim$2687.5cm^{-1}, FWHM(2D) narrows from$\sim$56.6cm^{-1} to$\sim$32.5cm^{-1}, Fig.14c. I(2D)/I(G) and A(2D)/A(G) are$\sim$5.1 and 10.7, indicating n-doping with E_F $\sim$100meV[133, 134] which corresponds to a carrier concentration$\sim 0.7\times10^{12}$cm^{-2}[133]. I(D)/I(G)$\sim$5.2 gives a defect density$\sim 1.4\times10^{12}$cm^{-2}[135, 136] for excitation energy 2.41eV and E_F $\sim$100meV. E_F estimated from A(2D)/A(G) would imply Pos(G)$\sim$1583.8cm^{-1} for unstrained graphene[133]. However in our experiment Pos(G)$\sim$1587.4cm^{-1}, which would imply a contribution from uniaxial (biaxial) strain$\sim$0.15% (0.05%)[137].

Bendable devices, able to coordinate with body motions, such as arms' and legs' bending or extension, are appealing for wearable electronics. Thus, we test I_{photo} as function of bending using a Deben Microtest setup, Fig.15f. The bending radius R_b is defined as[178]:

$$R_b = \frac{y^2 + (x/2)^2}{2y} \quad (18)$$

where y is the height at the chord midpoint and x is the chord circumference connecting the two ends of the grips, Fig.15f. To compare the performance at different R_b, the photocurrent at each R_b ($I_{Photo\ Bend}$) is normalized to that measured in flat conditions ($I_{Photo\ Rest}$). Fig.15d shows a change$\sim$ 17% of $\frac{I_{Photo\ Bend}}{I_{Photo\ Rest}}$ for R_b from flat to 25mm. This is comparable to that reported for LMs-based PDs, such as InSe PDs on PET[179], but in Ref.[179] R_{ext} was$\sim$50% that of R_b=30mm[179]. Comparable R_b was reported for flexible ZnO nanowires[180]

Accepted Manuscript

with on/off ratio$\sim 11\times10^4$ (I_d $\sim$120nA) under$\sim$4.5 mWcm^{-2} of UV light (R_{ext} not reported)[180]. However the operating voltage (1V) of our PDs is 3 times smaller than Ref.[180], making them more suitable for wearable applications, lowering power. The SLG/BP PDs performance as a function of bending cycles, where 1 bending cycle is set at R_b $\sim$35mm, is in Fig.15e. Our PDs retain$\sim$ 82% of $\frac{I_{Photo\ Bend}}{I_{Photo\ Rest}}$ for up to 30 cycles, comparable to what previously reported for CVD based MoS_2/SLG PDs on PET[181], making our approach promising for wearable and flexible applications.

DISCUSSION

Our PDs on Si/SiO_2 have R_{ext} up to$\sim$337A/W at 488nm for 1V bias and work in the range$\sim$488nm-2.7μm. Ref.[182] prepared PDs by depositing$\sim$30nm thick WS_2 by rubbing WS_2 powder against a polycarbonate substrate. Then, Au(100nm)/Ti(5nm) electrodes were made using e-beam evaporation through a shadow mask. The WS_2-based PDs showed R_{ext} $\sim$144mA/W at 625nm and V_{ds} $\sim$10V, worse than ours, because of the photoconductive gain enhancement in our inkjet-printed hybrid SLG/BP PDs. Ref.[183] presented WS_2-based PDs using$\sim$4nm WS_2 fabricated via RF magnetron sputtering, with R_{ext} $\sim$1.68mA/W at 405nm[183]. This is worse than ours because of the photoconductive gain mechanism in our hybrid SLG/BP PDs. Ref.[184] measured R_{ext} $\sim$0.16A/W at 405nm in self-powered PDs based on oxidized WS_2(O-WS_2)/WS_2 heterojunctions. $\sim$7.2nm WS_2 was transferred onto Si/SiO_2 by polydimethylsiloxane (PDMS)-assisted micromechanical exfoliation. Photoresist was then spin-coated on WS_2 via e-beam photolithography, followed by oxygen plasma irradiation to form selective oxidation regions. Then, Au(100nm)/Ti(10nm) electrodes were prepared by photolithography and electron beam deposition[184]. The fabrication process is more complex than ours, and the resulting R_{ext} is$\sim$2000 times lower, since no bias is applied through source and drain electrodes to dissociate photogenerated charges. Ref.[185] used spin-coated carbon QDs on CVD 1L-MoS_2 to achieve R_{ext} $\sim$377A/W at 360nm and 5V. While R_{ext} is comparable to ours, the PDs in Ref.[185] operate at 5V and only between 300-700nm, due to the spectral coverage of the carbon QDs[185], while our PDs work at 1V from 488nm to 2.7μm. Ref.[186] reported MoS_2-based PDs, prepared by abrasion of MoS_2 crystal (thickness$\sim$15-25μm) on the substrate, resulting in R_{ext} $\sim$1.5μA/W at 660nm and V_{ds} $\sim$20V. R_{ext} and operation voltage are worse than ours, because of our photoconductive gain, combined with the use of BP as photoactive material. To the best of our knowledge, our SLG/BP PD on Si/SiO_2 has the highest R_{ext} amongst inkjet-printed LMs based PDs and our operation wavelength range (488-2700nm) is the broadest, as summarized in Table I.

For SLG/BP PDs on fabric we get R_{ext} $\sim$6mA/W at 488nm, i.e.$\sim$56000 less than on SLG/BP PDs on Si/SiO_2 substrates. This R_{ext} decrease is expected, since the photogenerated h in the BP VP experience weaker electric fields at the SLG/BP interface (p-doping$\sim$270meV) compared to the SLG/BP interface (n-doping$\sim$360meV) on Si/SiO_2. Moreover, μ for SLG on fabric is lower than that on Si/SiO_2, and the channel in our PDs on fabric is$\sim$8 times larger than on Si/SiO_2. R_{ext} also decreases when the optical power increases, due to the increase in scattering of photogenerated carriers in the channel[166], and Auger recombination induced by increasing power[166].

To the best of our knowledge, there is no report of inkjet-printed textile PDs based on LMs. Our R_{ext} is$\sim$6 times higher than inkjet-printed SLG/WS_2 PDs on PET[43] and one order of magnitude higher (R_{ext} $\sim$0.11 mA/W at 405nm[101]) than CVD SLG based PDs on flexible (acrylic) substrates[101].

CONCLUSIONS

We reported an inkjet printing-based approach to prepare PDs, combining CVD SLG and binder-free LPE BP. The devices have R_{ext} up to$\sim$337A/W at 488nm, and$\sim$48mA/W at 2700nm, with operation voltage$\leq 1V$. We used this to prepare flexible PDs on polyester fabric. These PDs were investigated as function of bending radius and bending cycles. The responsivity, flexibility, and low operation voltage of our PDs makes them attractive for wearable and low-power optoelectronic applications.

ACKNOWLEDGMENTS

We acknowledge funding from EU grants Graphene Flagship, HiGraphInk, Neurofibres, ERC Grants Hetero2D, EPSRC Grants EP/K01711X/1, EP/K017144/1, EP/N010345/1, EP/L016087/1, EP/V000055/1, EP/P00119X/1, DSTL, ISF grant 1732/18.

* Present Address: Institute for Materials Discovery, University College London, Torrington Place, London, WC1E 7JE, UK

† present address: Institut fur Festkorperphysik, Friedrich Schiller Universitat Jena, 07743 Jena, Germany

‡ present address: School of Engineering, University of Greenwich, Central Avenue, Chatham Maritime, Kent, ME4 4TB, UK

§ acf26@eng.cam.ac.uk

[1] B. Fowler, C. Liu, S. Mims, J. Balicki, W. Li, H. Do, J. Appelbaum, and P. Vu, Proc. SPIE, **7536**, 753607 (2010).

Accepted Manuscript

[2] T. Mueller, F. Xia, and P. Avouris, Nat. Photonics **4**, 297 (2010).
[3] JE. Kallhammer, Nat. Photonics **5**, 12 (2006).
[4] V. Formisano, S. Atreya, T. Encrenaz, N. Ignatiev, M. Giuranna, Science **306**, 1758 (2004).
[5] F. H. L. Koppens, T. Mueller, Ph. Avouris, A. C. Ferrari, M. S. Vitiello, and M. Polini, Nat. Nanotechnol.**9**, 780 (2014).
[6] S. M. Sze and K. K. Ng, Physics of semiconductor devices, John wiley and sons (2006).
[7] M. Henini and M. Razeghi, Handbook of infrared detection technologies, Elsevier, 2002.
[8] D. AB. Miller, Proc. IEEE **88**, 728 (2000).
[9] J. Jiang, K. Mi, S. Tsao, W. Zhang, H. Lim, T. O'Sullivan, T. Sills, and M. Razeghi, Appl. Phys. Lett.**84**, 2232 (2004).
[10] W. Leia, J. Antoszewski, and L. Faraone, Appl. Phys. Lett.**2**, 041303 (2015).
[11] A. C. Ferrari, F. Bonaccorso, V. Falko, K. S. Novoselov, S. Roche, P. Bøggild, S. Borini, F. H. L. Koppens, V. Palermo, N. Pugno et al., Nanoscale **7**, 4598 (2015).
[12] G. Konstantatos, M. Badioli, L. Gaudreau, J. Osmond, M. Bernechea, F. P. G. De Arquer, F. Gatti, and F. H. Koppens, Nat. Nanotechnol **7**, 363 (2012).
[13] I. Nikitskiy, S. Goossens, D. Kufer, T. Lasanta, G. Navickaite, F. H. L. Koppens, and G. Konstantatos, Nat. Commun.**7**, 1 (2016).
[14] P. Ma, Y. Salamin, B. Baeuerle, A. Josten, W. Heni, A. Emboras, and J. Leuthold, ACS Photonics.**6**, 154 (2018).
[15] B. Y. Zhang, T. Liu, B. Meng, X. Li, G. Liang, X. Hu, and Q. J. Wang, Nat. Nanotechnol.**9**, 273 (2014).
[16] L. Viti, D. G. Purdie, A. Lombardo, A. C. Ferrari, and M. S. Vitiello, Nano Lett.**20**, 3169-3177 (2020).
[17] M. Asgari, E. Riccardi, O. Balci, D. De Fazio, S. M. Shinde, J. Zhang, S. Mignuzzi, F. H. L. Koppens, A. C. Ferrari, L. Viti, and M. S. Vitiello, ACS Nano**15**, 17966-17976 (2021).
[18] S. Goossens, G. Navickaite, C. Monasterio, S. Gupta, J. J. Piqueras, R. Pérez, G. Burwell, I. Nikitskiy, T. Lasanta, T. Galán, E. Puma, A. Centeno, A. Pesquera, A. Zurutuza, G. Konstantatos and F. Koppens , Nat. Photonics **11**, 366 (2017).
[19] H. Tan, Y. Fan, Y. Zhou, Q. Chen, W. Xu, and J. H. Warner, ACS nano**10**, 7866 (2016).
[20] T. Chen, Y. Sheng, Y. Zhou, R-J. Chang, X. Wang, H. Huang, Q. Zhang, L. Hou, and J. H. Warner, ACS Appl. Mater. Interfaces**11**, 6421 (2019).
[21] D. Kufer, I. Nikitskiy, T. Lasanta, G. Navickaite, F. H. L. Koppens, and G. Konstantatos, Adv. Mater. **27**, 176 (2015).
[22] N. Huo, and G. Konstantatos, Nat. Commun. **8**, 1 (2017).
[23] G. Konstantatos, Nat. Commun.**9**, 1 (2018).
[24] O. Özdemir, I. Ramiro, S. Gupta, and G. Konstantatos, ACS Photonics**6**, 2381 (2019).
[25] N. Huo, S. Gupta, and G. Konstantatos, Adv. Mater.**29**, 1606576 (2017).
[26] E. J. H. Lee, K. Balasubramanian, R. T. Weitz, M. Burghard, and K. Kern, Nat. Nanotechnol.**3**, 486 (2008).
[27] F. Bonaccorso, Z. Sun, T. Hasan, and A. C. Ferrari, Nat. Photonics **4**, 611 (2010).
[28] T. Kobayashia, M. Bando, N. Kimura, K. Shimizu, K. Kadono, N. Umezu, K. Miyahara, S. Hayazaki, S. Nagai, Y. Mizuguchi, Y. Murakami, and D. Hobara, Appl. Phys. Lett. **102**, 023112 (2013).
[29] D. Brida, A. Tomadin, C. Manzoni, Y. J. Kim, A. Lombardo, S. Milana, R. R. Nair, K. S. Novoselov, A. C. Ferrari, G. Cerullo, and M. Polini, Nat. Commun. **4**, 1 (2013).
[30] Y. Lee, J. Kwon, E. Hwang, C-H. Ra, W. J. Yoo, J-H. Ahn, J. H. Park, J. H. Cho, Adv. Mater.**27**, 41-46 (2015).
[31] C. Backes, Amr. M. Abdelkader, C. Alonso, A. Andrieux-Ledier, R. Arenal, J. Azpeitia, N. Balakrishnan, L. Banszerus, J. Barjon, R. Bartali et al., 2d Mater. **7**, 022001 (2020).
[32] Y. Hernandez, V. Nicolosi, M. Lotya, F. M. Blighe, Z. Sun, S. De, I. McGovern, B. Holland, M. Byrne, Y. K. Gun'Ko et al., Nat. Nanotechnol **3**, 563 (2008).
[33] F. Torrisi, T. Hasan, W. Wu, Z. Sun, A. Lombardo, T. S. Kulmala, G.-W. Hsieh, S. Jung, F. Bonaccorso, P. J. Paul, et al., ACS Nano **6**, 2992 (2012).
[34] P. G. Karagiannidis, S. A. Hodge, L. Lombardi, F. Tomarchio, N. Decorde, S. Milana, I. Goykhman, Y. Su, S. V. Mesite, D. N. Johnstone, R. K. Leary, P. A. Midgley, N. M. Pugno, F. Torrisi, A. C. Ferrari, ACS Nano **11**, 2742 (2017).
[35] F. Bonaccorso, A. Lombardo, T. Hasan, Z. Sun, L. Colombo, A. C. Ferrari, Mater. Today **15**, 564 (2012).
[36] H. Kaur, J. N. Coleman, Adv. Mater. **15**, 2202164 (2022).
[37] D. Dodoo-Arhin, R. C. Howe, G. Hu, Y. Zhang, P. Hiralal, A. Bello, G. Amaratunga, and T. Hasan, Carbon **105**, 33 (2016).
[38] J. Yang, D. Voiry, S. J. Ahn, D. Kang, A. Y. Kim, M. Chhowalla, and H. S. Shin, Angew Chem Int Ed Engl. **52**, 13751 (2013).
[39] F. Bonaccorso, L. Colombo, G. Yu, M. Stoller, V. Tozzini, A. C. Ferrari, R. S. Ruoff, V. Pellegrini, Science**347**, 1246501 (2015).
[40] J. Li, F. Ye, S. Vaziri, M. Muhammed, M. C. Lemme, and M. östling, Adv. Mater. **25**, 3985 (2013).
[41] D. J. Finn, M. Lotya, G. Cunningham, R. J. Smith, D. McCloskey, J. F. Donegan, and J. N. Coleman, J. Mater. Chem. C **2**, 925 (2014).
[42] G. Hu, T. Albrow-Owen, X. Jin, A. Ali, Y. Hu, R. C. Howe, K. Shehzad, Z. Yang, X. Zhu, R. I. Woodward, et al., Nat. Commun. **8**, 278 (2017).
[43] D. McManus, S. Vranic, F. Withers, V. Sanchez- Romaguera, M. Macucci, H. Yang, R. Sorrentino, K. Parvez, S.-K. Son, G. Iannaccone, et al., Nat. Nanotechnol. **12**, 343 (2017).
[44] K. Lee, H-Y. Kim, M. Lotya, J. N. Coleman, G-T. Kim, G. S. Duesberg, Adv. Mater. **23**, 4178 (2011).
[45] Y. Lee, J. Yang, D. Lee, Y-H. Kim, J-H. Park, H. Kim, and J. Ho Cho, Nanoscale **8**, 9193 (2016).
[46] R. F. Hossain, I. G. Deaguero, T. Boland, and A. B. Kaul, NPJ 2D Mater. Appl.**1**, 1 (2017).
[47] J. Li, M. M. Naiini, S. Vaziri, M. C. Lemme, and M. östling, Adv. Funct. Mater. **24**, 6524 (2014).
[48] J-W. T. Seo, J. Zhu, V. K. Sangwan, E. B. Secor, S. G. Wallace, and M. C. Hersam, Appl. Mater. Interfaces **11**, 5675 (2019).
[49] A. Morita, Appl. Phys. A**39**, 227 (1986).

Accepted Manuscript

[50] F. Xia, H. Wang, D. Xiao, M. Dubey, and A. Ramasubramaniam, Nat. Photonics**8**, 899 (2014).
[51] T-Y. Chang, P-L. Chen, J-H. Yan, W-Q. Li, Y-Y. Zhang, D-I. Luo, J-X. Li, K-P. Huang, and C-H. Liu, ACS Appl. Mater. Interfaces**12**, 1201 (2019).
[52] X. Chen, X. Lu, B. Deng, O. Sinai, Y. Shao, C. Li,S. Yuan, V. Tran, K. Watanabe, T. Taniguchi, et al., Nat. Commun. **8**, 1672 (2017).
[53] M. Buscema, D. J. Groenendijk, S. I. Blanter, G. A. Steele, H. S. J. van der Zant, and A. Castellanos-Gomez, Nano Lett.**14**, 3347 (2014).
[54] M. Huang, M. Wang, C. Chen, Z. Ma, X. Li, J. Han, and Y. Wu, Adv. Mater.**28**, 3481 (2016).
[55] L. Huang, B. Dong, X. Guo, Y. Chang, N. Chen, X. Huang, W. Liao, C. Zhu, H. Wang, C. Lee, and K-W. Ang, ACS Nano**13**, 913 (2018).
[56] J. Bullock, M. Amani, J. Cho, Y-Z. Chen, G. H. Ahn, V. Adinolfi, V. R. Shrestha, Y. Gao, K. B. Crozier, Y-L. Chueh, and A. Javey, Nat. Photonics**12**, 601 (2018).
[57] Q. Guo, A. Pospischil, M. Bhuiyan, H. Jiang, H. Tian, D. Farmer, B. Deng, C. Li, S.-J. Han, H. Wang, et al., Nano Lett. **16**, 4648 (2016).
[58] M. Engel, M. Steiner, and P. Avouris, Nano Lett. **14**, 6414 (2014).
[59] Y. Huang, Y-H. Pan, R. Yang, L-H. Bao, L. Meng, H-L. Luo, Y-Q. Cai, G-D. Liu, W-J. Zhao, Z. Zhou, et al., Nat. Commun.**11**, 1 (2020).
[60] K. S. Novoselov, A. K. Geim, S. Morozov, D. Jiang, M. Katsnelson, I. Grigorieva, S. Dubonos, and A. A. Firsov, Nature **438**, 197 (2005).
[61] A. Castellanos-Gomez, L. Vicarelli, E. Prada, J. O. Island, K. Narasimha-Acharya, S. I. Blanter, D. J. Groenendijk, M. Buscema, G. A. Steele, J. Alvarez, et al., 2D Mater. **1**, 025001 (2014).
[62] L. Kou, C. Chen, and S. C. Smith, J. Phys. Chem. Lett. **6**, 2794 (2015).
[63] J. B. Smith, D. Hagaman, and H-F. Ji, Nanotechnology **27**, 215602 (2016).
[64] D. Hanlon, C. Backes, E. Doherty, C. S. Cucinotta, N. C. Berner, C. Boland, K. Lee, A. Harvey, P. Lynch, Z. Gholamvand, et al., Nat. Commun. **6**, 8563 (2015).
[65] J. Kang, J. D. Wood, S. A. Wells, J.-H. Lee, X. Liu, K.-S. Chen, and M. C. Hersam, ACS Nano **9**, 3596 (2015).
[66] J. Kang, S. A. Wells, J. D. Wood, J-H. Lee, X. Liu, C. R. Ryder, J. Zhu, J. R. Guest, C. A. Husko, and M. C. Hersam, Proc. Natl. Acad. Sci.**113**, 11688 (2016).
[67] G. Zhou, Z.Li, Y. Ge, H. Zhang, and Z. Sun, Nanoscale Adv.**2**, 1059 (2020).
[68] H. Yuan, X. Liu, F.h Afshinmanesh, W. Li, G. Xu, J. Sun, B. Lian, A. G. Curto, G. Ye, Y. Hikita, Z. Shen, S-C. Zhang, X. Chen, M. Brongersma, H. Y. Hwang, and Y. Cui, Nat. Nanotechnol., **10**, 707 (2015).
[69] Y. Liu, B. N. Shivananju, Y. Wang, Y. Zhang, W. Yu, S. Xiao, T. Sun, W. Ma, H. Mu, S. Lin, et al., ACS Appl. Mater. Interfaces **9**, 36137 (2017).
[70] T-Y. Kim, J. Ha, K. Cho, J. Pak, J. Seo, J. Park, J-K. Kim, S. Chung, Y. Hong, and T. Lee, ACS Nano**11**, 10273 (2017).
[71] F. Withers, H. Yang, L. Britnell, A. P. Rooney, E. Lewis, A. Felten, C. R. Woods, V. Sanchez Romaguera, T. Georgiou, A. Eckmann, Y. J. Kim, S. G. Yeates, S. J. Haigh, A. K. Geim, K. S. Novoselov, and C. Casiraghi, Nano Lett. **14**, 3987 (2014).
[72] J. Miao, B. Song, Q. Li, L. Cai, S. Zhang, W. Hu, L. Dong, and C. Wang, ACS Nano, **11**, 6048 (2017).
[73] B. E. Saleh and M. C. Teich, Fundamentals of photonics, john Wiley and sons, 2019.
[74] K. Pan, Y. Fan, T. Leng, J. Li, Z. Xin, J. Zhang, L. Hao, J. Gallop, K. S. Novoselov, and Z. Hu, Nat. Commun. **9**, 1 (2008).
[75] B. J. Carey, J. Z. Ou, R. M. Clark, K. J. Berean, A. Zavabeti, A. S. R. Chesman, S. P. Russo, D. W. M. Lau, Z-Q. Xu, Q. Bao, O. Kavehei, B. C. Gibson, M. D. Dickey, R. B. Kaner, T. Daeneke, and K. Kalantar-Zadeh, Nat. Commun. **8**, 1 (2017).
[76] M. Bariyam, Z. Shahpar, H. Park, J. Sun, Y. Jung, W. Gao, H. Y. Y. Nyein, T. S. Liaw, L-C. Tai, Q. P. Ngo, M. Chao, Y. Zhao, M. Hettick, G. Cho, and A. Javey, ACS Nano. **12**, 6978 (2018).
[77] A. Nathan, A. Ahnood, M. T. Cole, S. Lee, Y. Suzuki, P. Hiralal, F. Bonaccorso, T. Hasan, L. Garcia-Gancedo, A. Dyadyusha, et al., Proc. IEEE **100**, 1486 (2012).
[78] L. Yang, A. Rida, R. Vyas, and M. M. Tentzeris, IEEE Trans. Microw. Theory Tech. **55**, 2894 (2007).
[79] K. Jaakkola, V. Ermolov, P. G. Karagiannidis, S. A. Hodge, L. Lombardi, X. Zhang, R. Grenman, H. Sandberg, A. Lombardo, and A. C. Ferrari, 2D Mater. **7**, 015019 (2019).
[80] M. Tudorache and C. Bala, Anal. Bioanal. Chem. **388**, 565 (2007).
[81] J. Bharathan and Y. Yang, Appl. Phys. Lett.**72**, 2660 (1998).
[82] M. L. Hammock, A. Chortos, B. C.-K. Tee, J. B.-H. Tok, and Z. Bao, Adv. Mater. **25**, 5997 (2013).
[83] S. E. Shaheen, R. Radspinner, N. Peyghambarian, and G. E. Jabbour, Appl. Phys. Lett. **79**, 2996 (2001).
[84] X. Cao, H. Chen, X. Gu, B. Liu, W. Wang, Y. Cao, F. Wu, and C. Zhou, ACS Nano **8**, 12769 (2014).
[85] P. H. Lau, K. Takei, C. Wang, Y. Ju, J. Kim, Z. Yu, T. Takahashi, G. Cho, and A. Javey, Nano Lett. **13**, 3864 (2013).
[86] K. Higuchi, S. Kishimoto, Y. Nakajima, T. Tomura, M. Takesue, K. Hata, E. I. Kauppinen, and Y. Ohno, Appl. Phys. Express **6**, 085101 (2013).
[87] E. B. Secor, P. L. Prabhumirashi, K. Puntambekar, M. L. Geier, and M. C. Hersam, J. Phys. Chem. Lett. **4**, 1347 (2013).
[88] L. W. Ng, G. Hu, R. C. Howe, X. Zhu, Z. Yang, C. Jones, and T. Hasan,*Printing of Graphene and Related 2D Materials*(Springer, 2019).
[89] A. G. Kelly, T. Hallam, C. Backes, A. Harvey, A. S. Esmaeily, I. Godwin, J. Coelho, V. Nicolosi, J. Lauth, A. Kulkarni, S. Kinge, L. D. A. Siebbeles, G. S. Duesberg, and J. N. Coleman1, Science**356**, 69 (2017).
[90] H. Sirringhaus, T. Kawase, R. H. Friend, T. Shimoda, M. Inbasekaran, W. Wu, and E. P. Woo, Science **290**, 2123 (2000).
[91] T. Sekitani, Y. Noguchi, U. Zschieschang, H. Klauk, and T. Someya, PNAS **105**, 4976 (2008).
[92] G. Hu, L. W. T. Ng, X. Zhu, R. C. T. Howe, and T. Hasan, Chem. Soc. Rev.**47**, 3265 (2018).
[93] I. M. Hutchings and D. Graham ,*Inkjet Technology for Digital Fabrication*(John Wiley and Sons, 2012).
[94] Y-Y. Noh, N. Zhao, M. Caironi, and H. Sirringhaus, Nat. Nanotechnol. **2**, 784 (2007).
[95] T. Kawase, H. Sirringhaus, R. H. Friend, and T. Shimoda, Adv. Mater. **13**, 1601 (2001).

Accepted Manuscript

[96] J. A. Hondred, L. R. Stromberg, C. L. Mosher, and J. C. Claussen, ACS nano **11**, 9836 (2017).
[97] A. Favron, E. Gaufrès, F. Fossard, A.-L. PhaneufL-Heureux, N. Y. Tang, P. L. Lévesquee, A. Loiseau, R. Leonelli, S. Francoeur, and R. Martel, Nat. Mater. **14**, 826 (2015).
[98] K. K. Kam, B. A. Parkinson, J. Phys. Chem. **86**, 463-467 (1982).
[99] A. Splendiani, L. Sun, Y. Zhang, T. Li, J. Kim, C-Y. Chim, G. Galli, and F. Wang, Nano Lett. **10**, 1271-1275 (2010).
[100] S. Wang, P. K. Ang, Z. Wang, A. L. L. Tang, J. T. L. Thong, and K. P. Loh, Nano Lett. **10**, 92-98 (2010).
[101] P. Kang, M. C. Wang, P. M. Knapp, and S. Nam, Adv. Mater. **28**, 4639 (2016).
[102] F. Bonaccorso, T. Hasan, P. H. Tan, C. Sciascia, G. Privitera, G. Di Marco, P. G. Gucciardi, and A. C. Ferrari, J. Phys. Chem. C.**114**, 17267 (2010).
[103] H. Liu, A. T. Neal, Z. Zhu, Z. Luo, X. Xu, D. Tománek, and Peide D. Ye, ACS Nano **8**, 4033 (2014).
[104] F. Xia, H. Wang, and Y. Jia, Nat. Commun. **5**, 1 (2014).
[105] Y. Akahama, M. Kobayashi, and H. Kawamura, Solid State Commun. **104**, 311 (1997).
[106] X. Wang, N. Mao, W. Luo, H. Kitadai, and X. Ling, J. Phys. Chem. Lett.**9**, 2830 (2018).
[107] H. B. Ribeiro, M. A. Pimentab, and C. J.S. de Matos, J. Raman Spectrosc **49**, 76 (2018).
[108] H. B. Ribeiro, C. E. P. Villegas, D. A. Bahamon, D. Muraca, A. H. Castro Neto, E. A. T. de Souza, A. R. Rocha, M. A. Pimenta and C. J. S. de Matos, Nat. Commun.**7**, 1 (2016).
[109] B. Derby and N. Reis, MRS Bull. **28**, 815 (2003).
[110] B. Derby, Annu. Rev. Mater. Res. **40**, 395 (2010).
[111] J. E. Fromm, IBM J. RES. DEV.**28**, 322 (1984).
[112] R. D. Deegan, O. Bakajin, T. F. Dupont, G. Huber, S. R. Nagel, and T. A. Witten, Nature **389**, 827 (1997).
[113] E. B. Secor, B. Y. Ahn, T. Z. Gao, J. A. Lewis, and M. C. Hersam, Adv. Mater. **27**, 6683 (2015).
[114] M. Lotya, Y. Hernandez, P. J. King, R. J. Smith, V. Nicolosi, L. S. Karlsson, F. M. Blighe, S. De, Z. Wang, I. McGovern, et al., J. Am. Chem. Soc. **131**, 3611 (2009).
[115] D. R. Lide et al., CRC Handbook of Chemistry and Physics**89**, 3 (2005).
[116] K.P.Lee, N. C. Chromey, R.Culik, J. R. Barnes, P. W. Schneider, Fund Appl Toxicol**9**, 222 (1987).
[117] https://apps.who.int/iris/handle/10665/42404
[118] S. Lin, S. Liu, Z. Yang, Y. Li, T. W. Ng, Z. Xu,Q .Bao, J. Hao, C.-S. Lee, C. Surya, et al., Adv. Funct. **26**, 864 (2016).
[119] J. D. Wood, S. A. Wells, D. Jariwala, K.-S. Chen, E. Cho, V. K. Sangwan, X. Liu, L. J. Lauhon, T. J. Marks, and M. C. Hersam, Nano Lett. **14**, 6964 (2014).
[120] N. B. Goodman, L. Ley, and D. Bullett, Phys. Rev. B **27**, 7440 (1983).
[121] J. Brunner, M. Thöler, S. Veprek, and R. Wild, J. Phys. Chem. Solids **40**, 967 (1979).
[122] J. V. Ashurst, T. M. Nappe, StatPearls Publishing (2019).
[123] L. Li, Y. Yu, G. J. Ye, Q. Ge, X. Ou, H. Wu, D. Feng, X. H. Chen, and Y. Zhang, Nat. Nanotechnol. **9**, 372 (2014).
[124] R. Bunsen, H. E. Roscoe, Ann. Phys. **162**, 235-263 (1857).
[125] A. Beer, Ann. Physik **162**, 78-88 (1852).
[126] R. Luther, A. Nikolopulos, Z. Phys. Chem. **82 U**, 361 (1913).
[127] D. F. Swinehart, J. Chem. Educ. **39**, 333 (1962).
[128] Y. Harada, K. Murano, I. Shirotani, T. Takahashi, Y. Maruyama, Solid State Commun.**44**, 877 (1982).
[129] A. A. Lagatsky, Z. Sun, T. S. Kulmala, R. S. Sundaram, S. Milana, F. Torrisi, O. L. Antipov, Y. Lee, J. H. Ahn, C. T. A. Brown, W. Sibbett, and A. C. Ferrari, Appl. Phys. Lett.**1**, 013113 (2013).
[130] S. Bae, H. Kim, Y. Lee, X. Xu, J.-S. Park, Y. Zheng, J. Balakrishnan, T. Lei, H. R. Kim, Y. I. Song, et al., Nat. Nanotechnol **5**, 574 (2010).
[131] A. C. Ferrari, J. Meyer, V. Scardaci, C. Casiraghi, M. Lazzeri, F. Mauri, S. Piscanec, D. Jiang, K. Novoselov, S. Roth, et al., Phys. Rev. Lett. **97**, 187401 (2006).
[132] A. C. Ferrari and D. M. Basko, Nat. Nanotechnol. **8**, 235 (2013).
[133] A. Das, S. Pisana, B. Chakraborty, S. Piscanec, S. K. Saha, U. V. Waghmare, K. S. Novoselov, H. R. Krishnamurthy, A. K. Geim, A. C. Ferrari, and A. K. Sood, Nat. Nanotechnol., **3**, 210 (2008).
[134] D. M. Basko, S. Piscanec, and A. C. Ferrari, Phys. Rev. B, **80**, 165413 (2009).
[135] L. G. Cançado, A. Jorio, E. M. Ferreira, F. Stavale, C. Achete, R. Capaz, M. Moutinho, A. Lombardo, T. Kulmala, and A. C. Ferrari, Nano Lett. **11**, 3190 (2011).
[136] M. Bruna, Anna K. Ott, M. Ijäs, D. Yoon, U. Sassi, and A. C. Ferrari, ACS Nano **8**, 7432 (2014).
[137] T. M. G. Mohiuddin, A. Lombardo, R. R. Nair, A. Bonetti, G. Savini, R. Jalil, N. Bonini, D. M. Basko, C. Galiotis, N. Marzari, K. S. Novoselov, A. K. Geim, and A. C. Ferrari, Phys. Rev. B**79**, 205433 (2009).
[138] D. Yoon, Y-W. Son, and H. Cheong, Phys. Rev. Lett.**106**, 155502 (2011).
[139] S. Pisana, M. Lazzeri, C. Casiraghi, K. S. Novoselov, A. K. Geim, A. C. Ferrari, and F. Mauri, Nat. Mater. **6**, 198 (2007).
[140] C. Casiraghi, S. Pisana, K. S. Novoselov, A. K. Geim, and A. C. Ferrari, Appl. Phys. Lett. **91**, 233108 (2007).
[141] C. Du, S. Wang, X. Miao, W. Sun, Y. Zhu, C. Wang, and R. Ma, Beilstein J. Nanotechnol.**10**, 2374 (2019).
[142] B. Jirgensons, J. Polym. Sci.**8**, 519 (1952).
[143] A. K. Geim and K. S. Novoselov, Nat. Mater. **6**, 183 (2007).
[144] J. Xia, F. Chen, J. Li, and N. Tao, Nat. Nanotech. **4**, 505 (2009).
[145] Y. Zhang, Y.-W. Tan, H. L. Stormer, and P. Kim, Nature **438**, 201 (2005).
[146] S. Adam, E. Hwang, V. Galitski, and S. D. Sarma, PNAS **104**, 18392 (2007).
[147] J.-H. Chen, C. Jang, S. Adam, M. Fuhrer, E. Williams, and M. Ishigami, Nat. Phys. **4**, 377 (2008).
[148] V. M. Galitski, S. Adam, and S. D. Sarma, Phys. Rev. B **76**, 245405 (2007).
[149] L-L. Chua, J. Zaumseil, J-F. Chang, E.C.-W. Ou, Peter K.-H. Ho, H. Sirringhaus, and R. H. Friend, Nature**434**, 194-199 (2005).
[150] K. Fukuda, T. Yokota, K. Kuribara, T. Sekitani, U. Zschieschang, H. Klauk, and T. Someya, Appl. Phys. Lett. **96**, 17 (2010).
[151] M. S. Mathur and N. A. Weir, J. Mol. Struct**15**, 459 (1973).
[152] J. Jakabovic, J. Kovacac, M. Weisb , D. Haskoc, R.Srnaneka, P. Valenta, R. Reseld, Microelectronics J

Accepted Manuscript

40, 595 (2009).
[153] T. Yamada, Y. Okigawa, M. Hasegawa, K. Watanabe, and T. Taniguchi **10**, 085309 (2020).
[154] I. Meric, M. Y. Han, A. F. Young, B. Ozyilmaz, P. Kim, and K. L. Shepard, Nat. Nanotechnol. **3**, 654 (2008).
[155] M. Lazzeri, S. Piscanec, F. Mauri, A. C. Ferrari, and J. Robertson, Phys. Rev. Lett.**95**, 236802 (2005).
[156] F. Xia, T. Mueller, R. Golizadeh-Mojarad, M. Freitag, Y-M. Lin, J. Tsang, V. Perebeinos, and P. Avouris, Nano Lett.**9**, 1039-1044 (2009).
[157] F. Xia, T. Mueller, Y-M. Lin, A. Valdes-Garcia, and P. Avouris, Nat. Nanotechnol.**4**, 839-843 (2009).
[158] P. Yasaei, B. Kumar, T. Foroozan, C. Wang, M. Asadi, D. Tuschel, J. E. Indacochea, R. F. Klie, A. Salehi-Khojin, Adv. Mater. **27**, 1887 (2015).
[159] J. D. Ingle Jr, S. R. Crouch,*Spectrochemical analysis*(1988).
[160] H. Liu, Y. Du, Y. Deng, P. D. Ye, Chem. Soc. Rev.**44**, 2732 (2015).
[161] V. Lucarini, J. J. Saarinen, K. E. Peiponen, E. M. Vartiainen,*Kramers-Kronig relations in optical materials research*(Springer, 2005).
[162] https://airekacells.com/blog/cuvette-guide
[163] E. Lampadariou, K. Kaklamanis,D. Goustouridis, I. Raptis, and E. Lidorikis, Chem. Soc. Rev.**9**, 499 (2022).
[164] G. W. Hanson, J. Appl. Phys.**44**, 084314 (2008).
[165] D. B. Velusamy, R. H. Kim, S. Cha, J. Huh, R. Khazaeinezhad, S. H. Kassani, G. Song, S. M. Cho, S. H. Cho, I. Hwang, J. Lee, K. Oh, H. Choi, and C. Park, Nat. Commun. **6**, 1 (2015).
[166] G. W. Mudd, S. A. Svatek, L. Hague, O. Makarovsky, Z. R. Kudrynskyi, C. J. Mellor, P. H. Beton, L. Eaves, K. S. Novoselov, Z. D. Kovalyuk, et al., Adv. Mater. **27**, 3760 (2015).
[167] Y. Fang, A. Armin, P. Meredith, and J. Huang, Nat. Photonics, **13**, 1 (2019).
[168] J, McCann and D. Bryson*Smart clothes and wearable technology*(Elsevier, 2009).
[169] J. W. S. Hearle, and W. E. Morton, *Physical properties of textile fibres*(Elsevier, 2008).
[170] P. A. Annis*Understanding and improving the durability of textiles*(Elsevier, 2012).
[171] *Preferred Fiber and Materials Market Report 2017*(Textile Exchange, 2019).
[172] N. Kim, S. Lienemann, I. Petsagkourakis, D. A. Mengistie, S. Kee, T. Ederth, V. Gueskine, P. Leclère, R. Lazzaroni, X. Crispin, and K. Tybrandt, Nat. Commun., **11**, 1 (2020).
[173] A. I. S. Neves, T. H. Bointon, L. V. Melo, S. Russo, I. de Schrijver, M. F. Cracium and H. Alves, Sci. Rep.**5**, 9866 (2015).
[174] G. Socrates *Infrared and Raman Characteristic Group Frequencies, 3rd*, John Wiley and Sons (2001).
[175] K. Bruckmoser, K. Resch, Macromol. Symp,**339**, 70 (2014).
[176] S. Parnell, K. Min, M. Cakmak, Polymer,**44**, 5137 (2003).
[177] A. T. Ezhil Vilian, S. An, S. R. Choe, C. H. Kwak, Y. S. Huh, J. Lee, Y-K. Han, Biosens. Bioelectron.,**86**, 122 (2016).
[178] J. W. S. Hearle, P. Grosberg, and Stanley Backer, *Structural mechanics of fibers, yarns, and fabrics*, Wiley-Interscience (1969).
[179] S. Reddy Tamalampudi, Y-Y. Lu, R. Kumar, R. Sankar, C-D. Liao, K. Moorthy, C-H. Cheng, F. Cheng, C-T. Chen, Nano Lett., **14**, 2800 (2014).
[180] S. Bai, W. Wu, Y. Qin, N. Cui, D. J. Bayerl, and X. Wang, Adv. Funct. Mater., **23**, 4464 (2011).
[181] D. De Fazio, I. Goykhman, D. Yoon, M. Bruna, A. Eiden, S. Milana, U. Sassi, M. Barbone, D. Dumcenco, K. Marinov, A. Kis, and A. C. Ferrari, ACS Nano.**10**, 8252 (2016).
[182] J. Quereda, S. Kuriakose, C. Munuera, F. J. Mompean, A. M. A. Enizi, A. Nafady, E. Diez, R. Frisenda, and A. Castellanos-Gomez, npj Flex. Electron, **6**, 1-9 (2022).
[183] B. H. Kim, H. H. Gu, and Y. J. Yoon, 2d Mater., **5**, 045030 (2018).
[184] J. Lu, Q. Ye, C. Ma, Z. Zheng, J. Yao, and G. Yang, ACS Nano, **8**, 12852-12865 (2022).
[185] H. Liu, F. Gao, Y. Hu, J. Zhang, L. Wang, W. Feng, J. Hou, and P. Hu, 2D Mater. , **6**, 035025 (2019).
[186] A. Mazaheri, M. Lee, H. S. J. van der Zant, R. Frisenda, and A. Castellanos-Gomez, **12**, 19068-19074 (2020).

Accepted Manuscript